Electron-cyclotron resonance heating and current drive source for flux-driven gyrokinetic simulations of tokamaks

P. Donnel [1,2], J.-B. Fontana [1], J. Cazabonne [1], L. Villard [1], S. Brunner [1], S. Coda [1], J. Decker [1], Y. Peysson[2]

[1] École Polytechnique Fédérale de Lausanne (EPFL), Swiss Plasma Center (SPC), CH-1015 Lausanne, Switzerland
[2] CEA, IRFM, Saint-Paul-Lez-Durance, F-13108, France

E-mail: `peter.donnel@cea.fr`

Abstract. Electromagnetic waves that resonate with the cyclotron motion of electrons in a magnetized plasma can efficiently transfer their momentum and energy to the plasma. This is routinely used to heat or to drive current in tokamak plasmas. The impact of this localized source of momentum and energy on turbulence and the retro-action of turbulence on the resonant interaction between the electromagnetic wave and the plasma have been scarcely studied due to the difficulty to simulate self-consistently the two physical mechanisms. In this paper a realistic source representing electron-cyclotron resonance heating (ECRH) and current drive (ECCD) is derived and implemented in a gyrokinetic code. The implementation of this realistic source in any existing global gyrokinetic code would enable the self-consistent study of turbulence in presence of ECRH/ECCD by this code. The analytical source derived in the paper is valid for a beam propagating in the equatorial plane of an axisymmetric tokamak plasma. The realistic ECRH/ECCD source is implemented in the global gyrokinetic code ORB5 and successfully benchmarked against an analytical theory [Albajar et al., PPCF, 2006] and the C3PO/LUKE suite of codes [Peysson et al., PPCF, 2011] which is routinely used to study ECRH/ECCD deposition.

1. Introduction

Electromagnetic waves can transfer their momentum and energy to magnetized plasmas. Efficient coupling between the wave and the plasma is possible in the presence of a resonance between the wave oscillation and the cyclotron motion of particles constituting the plasma. Electromagnetic waves with frequencies matching the Doppler shifted electron cyclotron (EC) frequency, or one of its harmonics, can be used to heat electrons, so-called Electron-Cyclotron Resonant Heating (ECRH), and/or to drive a current, so-called Electron-Cyclotron Current Drive (ECCD).

One of the main advantages of EC waves is their ability to couple with the plasma in a narrow region of space. Hence, EC waves can be used either as a pure heating/current source or to control MHD instabilities by accurately driving current at a precise position in the plasma.

It has been experimentally observed that, under certain conditions, suprathermal electrons generated by the EC power deposition are found in a region much larger than the region where the power deposition is expected using quasilinear drift-kinetic Fokker-Planck simulations [1, 2], solving beam propagation and power deposition in quiet plasmas. Two complementary improvements of models have therefore been proposed to reconcile these predictions with experimental observations. The first improvement is to take into account fluctuations of plasma density, induced by turbulence, along the path of the beam. These fluctuations, indeed, lead to the scattering of the beam and a, generally broadened, deposition area fluctuating in time. This effect has been studied with different approaches, starting from ray-tracing and drift-kinetic modeling [3, 4] to wave-kinetic modeling and full-wave studies [5, 6, 7, 8, 9], concluding that it can significantly broaden the power deposition profile, depending on the beam incidence onto the resonant layer and on the profile of density fluctuations.

The second improvement is to take into account the spatial transport of suprathermal electrons generated by the EC power deposition after the wave absorption. This has been first implemented as an ad-hoc additional transport term in drift-kinetic Fokker-Planck simulations [2, 10]. Comparison with experiments suggests that this transport is directly proportional to the diffusion in phase space induced by EC wave absorption. This ad-hoc transport allows to reconcile simulation predictions with experimental observations, suggesting that turbulence can efficiently transport suprathermal electrons generated by the EC power deposition. More generally, the possible synergies between EC power deposition and turbulence have not been studied so far. Indeed, to study these potential synergies, self-consistent simulations of turbulence in presence of ECRH/ECCD are required. To the best of our knowledge, this has never been done before, especially because of the difficulty to self-consistently treat turbulence and the resonant plasma/wave interaction. In this paper we derive an analytical operator modeling ECRH and ECCD. This operator can be used as a source term in any global gyrokinetic code, thus enabling the self-consistent simulation of turbulence in presence ECRH/ECCD. This is therefore a major step forward to study the possibility of synergistic effects between turbulence and ECRH/ECCD deposition.

In a recent paper [11], a quasilinear operator modeling a pure ECRH source in the specific case of a beam propagation in the equatorial plane of the tokamak was derived and implemented in the flux-driven gyrokinetic code ORB5 [12]. In this paper the generalization of this source to model both ECRH and ECCD, still assuming a propagation of the beam in the equatorial plane, is reported. This generalization of the source to include an ECCD component is an important step toward the perspective of comparing numerical results with experimental observations. Indeed, pure heating is a very particular case of the use of EC waves, and the presence of a current drive component is more relevant for applications foreseen in future large devices, such as MHD mode mitigation. Moreover, observation of suprathermal electrons using Hard X-Ray spectrometry is easier in ECCD configuration, as the resonance takes place farther away from the bulk distribution, exciting electrons with higher velocities and increasing the photon count rate at higher energies.

The derivation of the improved source term is presented in section 2. The numerical treatment of this quasi-linear operator is described in section 3. In section 4, numerical tests of this new source term are reported.

2. Derivation of an ECRH/ECCD source for a beam propagating on the midplane

The gyrokinetic equation can be symbolically written

$$\frac{\partial \bar{F}_s}{\partial t} + \left\{\bar{F}_s, \bar{H}_s\right\} = \sum_{s'} C\left(\bar{F}_s, \bar{F}_{s'}\right) + Q_{EC}\left(\bar{F}_s\right) + S\left(\bar{F}_s\right) \tag{1}$$

where $\bar{F}_s$ is the distribution function of gyro-centers of the species s. The second term of the left hand side is the Poisson bracket of $\bar{F}_s$ with the Hamiltonian $\bar{H}_s$. It corresponds to particle drifts and contains nonlinear terms, leading to turbulence. The first term on the right hand side is the collision operator, which is a key ingredient for the saturation of the EC beam deposition at large power, as it smooths out small scale fluctuations in the velocity space that are generated by the plasma/wave coupling. The term $Q_{EC}\left(\bar{F}_s\right)$ is the source term representing the ECRH/ECCD deposition which is derived in this paper. Note that it will be non zero only for electrons. Finally, the last term in Eq.1 represents other source and sink terms. Eq.1 needs to be solved for each species self-consistently with Poisson and Ampere equations to evolve the electromagnetic field.

The Larmor radius of electrons is small compared with the ion Larmor radius. As Ion Temperature Gradient (ITG) and Trapped Electron Mode (TEM) turbulence develop at typical space scales of the order of the ion Larmor radius, the drift kinetic approximation is regularly used for electrons in gyrokinetic codes. This implies that no distinction is made between the gyro-center and the particle electron distributions for the electrons. Finite Larmor radius effects will however be kept in the realistic source term Q_{EC}, as they are leading order terms of this operator.

The derivation of a quasilinear operator representing the coupling of an EC beam with a plasma has been presented in [11]. We give here the main results of the derivation. The interested reader is invited to read [11] for details of the computation. The operator describing the resonant coupling of an electromagnetic wave with the cyclotron motion of electrons reads

$$Q_{EC} = \sum_{n=-\infty}^{\infty} Q_n, \tag{2}$$

where n stands for the harmonic number and

$$Q_n = \nabla_{\mathbf{v}} \cdot \left[\mathbb{D}_n \cdot \nabla_{\mathbf{v}} F_e\right], \tag{3}$$

with F_e the particle electron distribution function and $\nabla_{\mathbf{v}}$ the standard nabla operator in velocity space. The diffusion matrix $\mathbb{D}_n$ is defined as

$$\mathbb{D}_n = D_n \mathbf{s}_n \mathbf{s}_n^T. \tag{4}$$

In Eq.4, the vector $\mathbf{s}_n$, which represents the direction of diffusion in the velocity space, is defined as

$$\mathbf{s}_n = \begin{pmatrix} s_n^{\perp} \\ s_n^{\parallel} \end{pmatrix} = \begin{pmatrix} -\frac{n\Omega_e}{\omega_b \gamma} \\ \lambda\left(v_\parallel, v_\perp\right) \frac{v_\perp}{c} \end{pmatrix}, \tag{5}$$

where $\Omega_e = eB/m_e$ is the non-relativistic electron cyclotron frequency with e the elementary charge and m_e the electron mass, ω_b is the beam frequency, γ is the

Lorentz factor, $v_\perp$ is the component of the velocity perpendicular to the magnetic field $\mathbf{B}$, c is the light speed and the function $\lambda\left(v_\parallel, v_\perp\right)$ is defined as

$$\lambda\left(v_\parallel, v_\perp\right) = \left(1 - \frac{n\Omega_e}{\gamma\omega_b}\right)\frac{c}{v_\parallel}, \tag{6}$$

with $v_\parallel$ the component of the velocity parallel to the magnetic field. For electrons, the main interaction is with negative harmonics. Indeed, with the conventions given in [11], the resonance condition reads $\omega_b = k_\parallel v_\parallel - n\Omega_e/\gamma$, with $k_\parallel$ the parallel component of the wave vector. As ω_b and Ω_e are positive, n needs to be negative to fulfill the resonance condition. An approximate version of the resonant diffusion coefficient has been derived in [11]. It reads

$$D_{-n} \simeq \tilde{D}_{-n} = \frac{\pi e^2 \mathcal{N}\left(\theta_0\right)}{2m_e^2\omega_b}\frac{c}{\left|v_\parallel\right|}\left|\mathbf{E}\right|^2 \frac{\sin\left(\theta_{\mathrm{res}}\right)\exp\left[-\left(\frac{\theta_{\mathrm{res}}-\theta_0}{\sigma}\right)^2\right]\mathcal{N}^2\left(\theta_{\mathrm{res}}\right)}{\int_0^\pi \sin\left(\theta\right)\exp\left[-\left(\frac{\theta-\theta_0}{\sigma}\right)^2\right]\mathcal{N}^2\left(\theta\right)d\theta}\left|\tilde{\Theta}^n_{k,res}\right|^2. \tag{7}$$

Eq.7 is rather general and relies on a few assumptions. The first one is the use of the cold plasma dispersion relation to express the plasma refractive index $\mathcal{N}$. This assumption is used to express the direction of the electric field, which enters in the definition of $\tilde{\Theta}^n_{k,res}$. The derivation of Eq.7 also assumes that the electric field intensity possesses a Gaussian shape of width W_0 in the direction perpendicular to its propagation. This leads to a Gaussian shape of the Fourier transform of the electric field in the direction perpendicular to its mean wavevector $\mathbf{k_0}$. The consequence of this assumption is found in the exponential functions in Eq.7. Indeed, θ_0 is the angle between the magnetic field and the mean wavevector of the beam $\mathbf{k_0}$, and $\sigma = 1/\left(k_0 W_0\right)$ is the width in the distribution of angles resulting from the finite width of the beam W_0. θ_{res} is the resonant angle corresponding to the matching of the Doppler shifted beam frequency with the cyclotron frequency or one of its harmonics. In Eq.7, $\mathbf{E}$ is the electric field of the beam and $\tilde{\Theta}^n_{k,res}$ is defined as

$$\tilde{\Theta}^n_{k,res} = \frac{\left[\begin{array}{c}\left[1+\mathcal{C}_1\left(\theta_{\mathrm{res}}\right)\right]J_{n+1}\left(\tilde{\rho}_{\mathrm{res}}\right)+\left[1-\mathcal{C}_1\left(\theta_{\mathrm{res}}\right)\right]J_{n-1}\left(\tilde{\rho}_{\mathrm{res}}\right)\\ -2\mathcal{C}_2\left(\theta_{\mathrm{res}}\right)\frac{v_\parallel}{v_\perp}J_n\left(\tilde{\rho}_{\mathrm{res}}\right)\end{array}\right]}{2\sqrt{1+\mathcal{C}_1\left(\theta_{\mathrm{res}}\right)^2+\mathcal{C}_2\left(\theta_{\mathrm{res}}\right)^2}}, \tag{8}$$

where J_n is the n-th Bessel function of first kind of argument $\tilde{\rho}_{\mathrm{res}} = \sin\left(\theta_{\mathrm{res}}\right)\mathcal{N}\left(\theta_{\mathrm{res}}\right)\omega_b v_\perp\gamma/\left(\Omega_e c\right)$ is a normalized Larmor radius, and

$$\mathcal{C}_1\left(\theta\right) = \frac{\mathcal{T}}{\mathcal{S}-\mathcal{N}^2\left(\theta\right)}, \tag{9}$$

$$\mathcal{C}_2\left(\theta\right) = \frac{\mathcal{N}^2\left(\theta\right)\cos\left(\theta\right)\sin\left(\theta\right)}{\mathcal{P}-\mathcal{N}^2\left(\theta\right)\sin^2\left(\theta\right)}. \tag{10}$$

Note that if one neglects finite Larmor radius ($\tilde{\rho}_{\mathrm{res}} = 0$), all Bessel functions are equal to zero except J_0. The consequence is that no absorption is possible except for the fundamental resonance. This is consistent with the fact that ECRH/ECCD deposition relies on a resonance between the electromagnetic wave and the cyclotron motion. The coefficients $\mathcal{P}$, $\mathcal{S}$ and $\mathcal{T}$ are the "Stix coefficients" which are related to the plasma dispersion relation. They are defined as $\mathcal{P} = 1 - \left(\omega_p/\omega_b\right)^2$, where $\omega_p = \sqrt{N_e e^2/\left(\epsilon_0 m_e\right)}$ is the plasma frequency, $\mathcal{S} = \left(\mathcal{R}+\mathcal{L}\right)/2$, $\mathcal{T} = \left(\mathcal{R}-\mathcal{L}\right)/2$, where $\mathcal{R} = \left(\mathcal{P}-\Omega_e/\omega_b\right)/\left(1-\Omega_e/\omega_b\right)$ and $\mathcal{L} = \left(\mathcal{P}+\Omega_e/\omega_b\right)/\left(1+\Omega_e/\omega_b\right)$.

The quasilinear operator Eq.7, derived in [11], requires as an input some characteristic quantities of the beam (beam waist W_0, mean wavevector of the beam $\mathbf{k_0}$ as well as the power carried by the beam along its path, which is proportional to the square of the electric field of the beam integrated over a surface perpendicular to the beam propagation direction). These quantities can in principle be evaluated by coupling a code computing the beam quantities (i.e. a ray-tracing code) with a global gyrokinetic code. But the coupling of such codes is numerically challenging. To avoid the coupling of another code with the gyrokinetic code, the particular case of a propagation of the beam in the equatorial plane of an axisymmetric plasma is assumed. This assumption can be fulfilled or not depending on the experimental setup (position of the launcher and direction of injection). In [11], a pure ECRH case is considered ($\theta_0 = \pi/2$), leading to an one-dimensional beam propagation (along the major radius). However, the pure ECRH case is really specific and a generalization of the model to treat both ECRH and ECCD cases is required before envisaging a comparison with experiments. In this paper, the model is generalized by assuming an axisymmetric plasma. This makes the beam propagation 2D (in the equatorial plane), but still analytical, see section 2.2. The breaking of the axisymmetry, for instance by magnetic ripple or resonant magnetic perturbations is experimentally possible. But axisymmetry assumption, in addition to considering a beam of constant width W_0 and to neglecting the poloidal magnetic field (i.e. $B_\theta \ll B_\varphi$), make it easier to have analytical models for the beam propagation. The possibility to include at the same time ECRH and ECCD requires a model, much more complex than the one for a pure ECRH case, to compute the power carried by the beam. Such a model has been derived by [13] and is presented in the subsection 2.4.

The rest of this section is organized as follows. In subsection 2.1, an analytical evaluation of the resonant angle θ_{res} is performed. It allows an efficient implementation compared with the binary search used in [11]. A similar computation, described in subsection 2.2, allows the computation of the beam path in the equatorial plane, and so of the mean angle θ_0 between the beam wave-vector and the plasma magnetic field. Once θ_{res} and θ_0 are evaluated, the remaining difficulty consists of expressing the spatial distribution of the beam electric field $\mathbf{E}$. To do so, the link between the beam electric field $\mathbf{E}$ and the power crossing a surface of constant major radius $P(R)$ is established in subsection 2.3. An analytical model, described in subsection 2.4, is used to evaluate the beam power along its path.

2.1. Evaluation of the resonant angle

The resonant angle θ_{res}, appearing in Eq.7, is the solution of the resonance condition $\omega_b = k_\parallel v_\parallel - n\Omega_e/\gamma$ which can be rewritten as [11]

$$\mathcal{N}\left(\theta_{\text{res}}\right)\cos\left(\theta_{\text{res}}\right) = \lambda\left(v_\parallel, v_\perp\right). \tag{11}$$

The cold plasma dispersion relation $\mathcal{N}(\theta)$ reads

$$\mathcal{N}^2_{O/X}(\theta) = \frac{\left(\mathcal{RL} + \mathcal{SP}\right)\tan^2\theta + 2\mathcal{SP} \pm \mathcal{G}_\theta}{2\left(\mathcal{S}\tan^2\theta + \mathcal{P}\right)}, \tag{12}$$

where O and X stand for the O-mode polarization and X-mode polarization respectively and

$$\mathcal{G}_\theta = \text{sign}\left(\omega_\text{b} - \Omega_\text{e}\right)\sqrt{\left(\mathcal{SP} - \mathcal{RL}\right)^2\tan^4\theta + \mathcal{P}^2\left(\mathcal{L} - \mathcal{R}\right)^2\left(\tan^2\theta + 1\right)}. \tag{13}$$

Note that the definition of $\mathcal{G}_\theta$ has been generalized compared with the one in [11] to include the unusual case $\omega_b < \Omega_e$, corresponding to a configuration of injection from the high field side and a coupling at the fondamental resonance. Defining $y = \cos(2\theta_{\rm res})$ and by squaring Eq.11, it is possible to show that y is the solution of

$$\begin{aligned}&(\mathcal{RL}+\mathcal{SP})\left(1-y^2\right)+2\mathcal{SP}\left(1+y\right)^2-4\lambda^2\left[\mathcal{S}\left(1-y\right)+\mathcal{P}\left(1+y\right)\right]=\\&\qquad\pm\left(1+y\right)\sqrt{\left(\mathcal{SP}-\mathcal{RL}\right)^2\left(1-y\right)^2+8\mathcal{P}^2\mathcal{T}^2\left(1+y\right)}.\end{aligned}\tag{14}$$

By squaring Eq.14 and using the definitions of the Stix coefficients, a long but straightforward computation allows one to compute the angle of resonance for the X-mode

$$\begin{aligned}\theta^X_{\rm res}&=\frac{1}{2}\arccos\left[x_+\left(\lambda^2\right)\right]\qquad \text{if } \lambda\geq 0\\&=\pi-\frac{1}{2}\arccos\left[x_+\left(\lambda^2\right)\right] \text{ if } \lambda<0\end{aligned}\tag{15}$$

and the O-mode

$$\begin{aligned}\theta^O_{\rm res}&=\frac{1}{2}\arccos\left[x_-\left(\lambda^2\right)\right]\qquad \text{if } \lambda\geq 0\\&=\pi-\frac{1}{2}\arccos\left[x_-\left(\lambda^2\right)\right] \text{ if } \lambda<0\end{aligned}\tag{16}$$

with

$$\begin{aligned}x_\pm\left(y\right)=&\left\{\mathcal{P}^2\left(2y-\mathcal{P}\right)+\left(\frac{\Omega_e}{\omega_b}\right)^2\left[\mathcal{P}\left(1-y\right)^2-y^2\right]\right.\\&\left.\pm\frac{\Omega_e}{\omega_b}\left(1-\mathcal{P}\right)y\sqrt{\left(\frac{\Omega_e}{\omega_b}\right)^2\left(1-y\right)^2+4\mathcal{P}y}\right\}/\\&\left\{\mathcal{P}\left[\mathcal{P}^2-\left(\frac{\Omega_e}{\omega_b}\right)^2\right]+y\left(\frac{\Omega_e}{\omega_b}\right)^2\left(\mathcal{P}-1\right)\right\}.\end{aligned}\tag{17}$$

2.2. Model for the spatial dependence of θ_0

The spatial dependence of the mean angle $\theta_0(R)$, appearing in Eq.7, also needs to be evaluated. To do so, we use the general expression which is implemented in the ray-tracing code C3PO [14]. The toroidal mode number of the beam is defined as $\tilde{n} = R\mathbf{e}_\varphi \cdot \mathbf{k}_0$ where $\mathbf{e}_\varphi$ is the toroidal direction and $\mathbf{k}_0$ is the mean wave vector associated with the beam. For an axisymmetric magnetic configuration, $\tilde{n}$ is invariant along the ray trajectory [14]. By neglecting the poloidal component of the magnetic field, we obtain

$$\mathcal{N}\left(\theta_0\right)\cos\left(\theta_0\right)=\frac{R_{in}}{R}\mathcal{N}\left(\theta_{0,in}\right)\cos\left(\theta_{0,in}\right),\tag{18}$$

where $\theta_{0,in} = \theta_0(R_{in})$ is the injection angle at the injection major radius R_{in}, where the beam is entering the plasma. Eq.18 has the same structure as Eq.11. Therefore the mean angle is given for a X-mode beam by

$$\begin{aligned}\theta^X_0&=\frac{1}{2}\arccos\left[x_+\left(\left[\frac{R_{in}}{R}\mathcal{N}\left(\theta_{0,in}\right)\cos\left(\theta_{0,in}\right)\right]^2\right)\right]\qquad\text{if } \lambda\geq 0\\&=\pi-\frac{1}{2}\arccos\left[x_+\left(\left[\frac{R_{in}}{R}\mathcal{N}\left(\theta_{0,in}\right)\cos\left(\theta_{0,in}\right)\right]^2\right)\right]\text{ if } \lambda<0\end{aligned}\tag{19}$$

and for a O-mode beam by

$$
\begin{aligned}
\theta_0^O &= \frac{1}{2}\arccos\left[x_-\left(\left[\frac{R_{in}}{R}\mathcal{N}\left(\theta_{0,in}\right)\cos\left(\theta_{0,in}\right)\right]^2\right)\right] && \text{if } \lambda \geq 0 \\
&= \pi - \frac{1}{2}\arccos\left[x_-\left(\left[\frac{R_{in}}{R}\mathcal{N}\left(\theta_{0,in}\right)\cos\left(\theta_{0,in}\right)\right]^2\right)\right] && \text{if } \lambda < 0
\end{aligned}
\tag{20}
$$

with $x_\pm$ defined by Eq.17. It is noteworthy that, for a perpendicular injection $\theta_{0,in} = \pi/2$, the mean angle is constant $\theta_0\left(R\right) = \pi/2 \quad, \forall R$. This specific case was used in [11] for the pure ECRH case.

2.3. Spatial dependence of the electric field in the case of a beam propagating in the equatorial plane

The power crossing a surface with a major radius R reads

$$
\begin{aligned}
P\left(R\right) &= R\int_0^{2\pi} d\varphi \int_{-\infty}^{\infty} dZ \frac{\epsilon_0\left|\mathbf{E}\right|^2}{2}\mathbf{v}_g\cdot\mathbf{e}_R \\
&= \frac{1}{2}R\epsilon_0\left|v_g\right|\sin\left(\theta_0\right)\int_0^{2\pi} d\varphi\int_{-\infty}^{\infty} dZ\left|\mathbf{E}\right|^2,
\end{aligned}
\tag{21}
$$

Note that the electric field is implicitly taken at the major radius R. Consistently with the assumption used to derive Eq.7, we assume that the beam has a Gaussian distribution of width W_0 perpendicular to its propagation direction

$$
\left|\mathbf{E}\right|^2 = \left|\mathbf{E}_{00}\left(s\right)\right|^2\exp\left[-\left(\frac{X}{W_0}\right)^2\right]\exp\left[-\left(\frac{Z}{W_0}\right)^2\right], \tag{22}
$$

where X is the coordinate in the direction perpendicular to the beam propagation in the equatorial plane and Z is the coordinate in the vertical direction. s stands for the arc length along the beam path from the injection location to the local position and $\left|\mathbf{E}_{00}\left(s\right)\right|^2$ is the maximum amplitude of the electric field at this arc length. When integrating the electric field on a surface of constant major radius R, s and X are such that the beam is evaluated on the surface of constant major radius R as illustrated by Fig.1. Because we assume a propagation at the equatorial plane, and because the width of the beam is small compared to the size of the plasma, the integration in the vertical direction is trivial and gives

$$
P\left(R\right) = \frac{\sqrt{\pi}}{2}RW_0\epsilon_0\left|v_g\right|\sin\left(\theta_0\right)\int_0^{2\pi} d\varphi\left|\mathbf{E}_{00}\left(s\right)\right|^2\exp\left[-\left(\frac{X}{W_0}\right)^2\right]. \tag{23}
$$

The integration in the direction φ is more challenging. In reality the EC beam is toroidally localised. However, assuming that the power deposited is quickly spread along the toroidal direction, we shall assume that the deposition is axisymmetric. This will have the advantage, in the context of a PIC code, to increase the sampling statistics. We then define a mean value for the electric field on the equatorial plane $\bar{E}\left(R\right)$ such that

$$
\bar{E}^2 = \frac{1}{2\pi}\int_0^{2\pi} d\varphi\left|\mathbf{E}_{00}\left(s\right)\right|^2\exp\left[-\left(\frac{X}{W_0}\right)^2\right], \tag{24}
$$

and so

$$
P\left(R\right) = \pi^{3/2}RW_0\epsilon_0\left|v_g\right|\sin\left(\theta_0\right)\bar{E}^2. \tag{25}
$$

We also define $\hat{E}$ such that

$$|\mathbf{E}|^2 = \hat{E}^2 \exp\left[-\left(\frac{Z}{W_0}\right)^2\right]. \tag{26}$$

We assume that $W_0 \ll R$, and define a new coordinate X' which corresponds to the coordinate on the surface R (see Fig.1). By noting that $X' \sin\theta_0 = X$ and by imposing that $\hat{E}$ be independent of θ_0 (in the absence of absorption), one gets $\bar{E} = \sin(\theta_0)\,\hat{E}$ and so

$$|\mathbf{E}|^2 = \frac{P(R)}{\pi^{3/2} R W_0 \epsilon_0 |v_g| \sin^3(\theta_0)} \exp\left[-\left(\frac{Z}{W_0}\right)^2\right]. \tag{27}$$

Eq.27 links the amplitude of the electric field to the power crossing the surface of constant major radius $P(R)$ and the group velocity v_g, whose expression is derived in the appendix A.

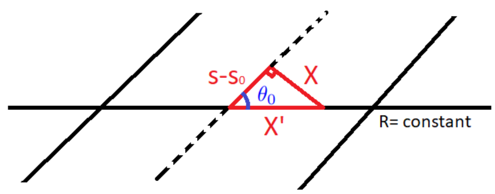

Figure 1. Link between X and X' coordinates.

2.4. *Model of absorption for an oblique propagation*

To evaluate the evolution of the beam power along its path, we use the quasi-exact analytical evaluation derived in [13]. The power is then related to the optical thickness of the plasma τ

$$P(R) = P_{in} \exp[-\tau(R)], \tag{28}$$

where $P_{in} = P(R_{in})$ is the injected power and τ is defined as the integral of the absorption coefficient α along the beam path $\tau = \int_0^L \alpha ds = \int_{R_{in}}^R \alpha |\sin(\theta_0) dR'|$. The absorption coefficient is given by

$$\alpha = \sum_{n \geq n_0} \alpha_n, \tag{29}$$

with

$$\alpha_n = \frac{\omega_p^2}{c\Omega_e} \frac{\pi}{2} \frac{\mu^2}{n_0 K_2(\mu)} P_n \exp\left[-\frac{n\mu}{n_0\sqrt{1-\mathcal{N}_\parallel^2}}\right] \sqrt{\left(\frac{n}{n_0}\right)^2 - 1}, \tag{30}$$

where $n_0 = \frac{\omega_b}{\Omega_e}\sqrt{1-\mathcal{N}_\parallel^2}$, $\mu = \frac{m_e c^2}{T_e}$, K_2 is the modified Bessel function of the second kind of order two, $\mathcal{N}_\perp = \mathcal{N}(\theta)\sin\theta$ and $\mathcal{N}_\parallel = \mathcal{N}(\theta)|\cos\theta|$.

In practice, for all cases of interest the limit $\mu \gg 1$ holds. Within this limit, the sum in Eq.30 is very well approximated by its first non zero component ($n = \lceil n_0 \rceil$)

which then corresponds to the harmonic of the beam considered. Moreover, one can use the fact that $\lim_{x\to\infty}\left[K_2(x)\exp(x)\right]=\sqrt{\frac{\pi}{2x}}$ to approximate the coefficient α_n

$$\alpha_n \simeq \tilde{\alpha}_n = \frac{\omega_p^2}{c\Omega_e}\sqrt{\frac{\pi}{2}}\frac{\mathcal{F}_n(\mu)}{n_0}\sqrt{\left(\frac{n}{n_0}\right)^2-1}, \tag{31}$$

where

$$\mathcal{F}_n(\mu) = \mu^{5/2}P_n\exp\left[\mu\left(1-\frac{n}{n_0\sqrt{1-\mathcal{N}_\parallel^2}}\right)\right]. \tag{32}$$

The function P_n is defined as

$$P_n = \pi\frac{(2n+1)!}{(2^n n!)^2}\left(\frac{n\Omega_e}{\omega_b\mathcal{N}_\perp}\right)^2\left[\mathcal{A}\left(\frac{\left|J_{n+1/2}(z_n)\right|^2}{x_n}\right)+\mathcal{B}\left(\frac{\left|J_{n+3/2}(z_n)\right|^2}{x_n}\right)\right], \tag{33}$$

where

$$\begin{aligned}\mathcal{A}(\cdot) &= \left(|A_{xz}|^2+|\hat{e}_y|^2\right)\cdot + \Re\left(iA_{xz}\hat{e}_y^*\right)\frac{x_n}{n}\frac{\partial\cdot}{\partial x_n}\\ &-\left(\frac{x_n}{n}\right)^2\frac{n}{n+1}|\hat{e}_y|^2\left(\cdot-\frac{\partial^2\cdot}{\partial y_n^2}\right)+\left(\frac{x_n}{n\sqrt{1-\mathcal{N}_\parallel^2}}\right)^2|\hat{e}_z|^2\frac{\partial^2\cdot}{\partial y_n^2}\\ &-\frac{x_n\left(2\Re\left(A_{xz}\hat{e}_z^*\right)+\Re\left(i\hat{e}_y^*\hat{e}_z\right)\frac{x_n}{n}\frac{\partial}{\partial x_n}\right)}{n\sqrt{1-\mathcal{N}_\parallel^2}}\frac{\partial\cdot}{\partial y_n},\end{aligned} \tag{34}$$

and

$$\mathcal{B}(\cdot) = \left(\frac{x_n}{n}\right)^2\frac{2n+3}{(n+1)(n+2)}|\hat{e}_y|^2\left(\cdot-\frac{\partial^2\cdot}{\partial y_n^2}\right), \tag{35}$$

In these expressions, A_{xz} is defined as

$$A_{xz} = \hat{e}_x + \frac{\mathcal{N}_\perp\mathcal{N}_\parallel}{1-\mathcal{N}_\parallel^2}\hat{e}_z, \tag{36}$$

and the quantities x_n, y_n are respectively defined as

$$x_n = \frac{\omega_b}{\Omega_e}\mathcal{N}_\perp\sqrt{\left(\frac{n}{n_0}\right)^2-1}, \tag{37}$$

$$y_n = \frac{\mu\mathcal{N}_\parallel}{\sqrt{1-\mathcal{N}_\parallel^2}}\sqrt{\left(\frac{n}{n_0}\right)^2-1}, \tag{38}$$

and the complex argument of the Bessel functions z_n is defined as

$$z_n = \frac{1}{2}\left(\sqrt{4x_n^2-y_n^2}+iy_n\right). \tag{39}$$

The derivatives of the function $\frac{\left|J_{m+1/2}(z_n)\right|^2}{x_n}$ with respect to x_n and y_n, which are necessary to evaluate Eq.34 and Eq.35, are derived analytically in appendix B.

The use of the cold plasma limit allows one to link the different components of the normalized wave electric field $\hat{\mathbf{e}} = \mathbf{E}_{\mathbf{k}}/\sqrt{|\mathbf{S}|/\epsilon_0 c}$. Indeed one has

$$i\frac{\hat{e}_y}{\hat{e}_x} = i\frac{E_{\mathbf{k},y}}{E_{\mathbf{k},x}} = \frac{\mathcal{T}}{\mathcal{S}-\mathcal{N}^2} \tag{40}$$

and

$$\frac{\hat{e}_z}{\hat{e}_x} = \frac{E_{\mathbf{k},z}}{E_{\mathbf{k},x}} = -\frac{\mathcal{N}_\parallel \mathcal{N}_\perp}{\mathcal{P}-\mathcal{N}_\perp^2} \tag{41}$$

In the cold plasma limit, the electromagnetic energy flux $\mathbf{S}$ is well approximated by the Poynting vector and leads us to express

$$|\hat{e}_y|^2 = \frac{1}{\mathcal{N}(\theta)\sqrt{a^2(\theta)+b^2(\theta)}} \tag{42}$$

with

$$a(\theta) = \left[1+\mathcal{P}\left(\frac{\mathcal{N}_\parallel \omega_b\left[\omega_p^2-\left(\omega_b^2-\Omega_e^2\right)\left(1-\mathcal{N}^2\right)\right]}{\Omega_e\omega_p^2\left(\mathcal{P}-\mathcal{N}_\perp^2\right)}\right)^2\right]\sin\theta \tag{43}$$

and

$$b(\theta) = \left|1+\frac{\mathcal{P}}{\mathcal{P}-\mathcal{N}_\perp^2}\left(\frac{\omega_b\left[\omega_p^2-\left(\omega_b^2-\Omega_e^2\right)\left(1-\mathcal{N}^2\right)\right]}{\Omega_e\omega_p^2}\right)^2\right||\cos\theta| \tag{44}$$

For the computation, one can assume without loss of generality that $\hat{e}_y$ is real and positive. Then using Eq.40 and Eq.41, one obtains that $\hat{e}_x$ and $\hat{e}_z$ are purely imaginary quantities.

For the specific case of an O-mode close to perpendicular propagation, one has $\mathcal{N}_\perp \simeq \mathcal{N} \simeq \mathcal{P}$ and then equations 41, 43 and 44 are not properly defined. For this specific case, one can approximate $\hat{e}_x = \hat{e}_y = 0$ and $\hat{e}_z = \mathcal{P}^{-1/2}$.

Note that for oblique propagation, with low temperature, the numerical evaluation of Eq.32 is challenging as it involves the multiplication of very large numbers with very small ones. To circumvent this difficulty, one can use the logarithm to perform the multiplication and then exponentiate the result.

3. Numerical implementation of the source term

In the previous section, the model for the quasi-linear operator representing the ECRH/ECCD source has been derived. In this section, the numerical implementation of this source term in the global gyrokinetic code ORB5 is detailed. In subsection 3.1, the drag term is analytically derived, avoiding a difficult numerical evaluation of this term. The markers with a low parallel velocity are displaying a diverging drag term. To avoid this divergence, the numerical treatment of these markers is different from the one of the other markers. This treatment is detailed in subsection 3.2. Finally, the adaptation of the source term to the usage of "heavy electrons", often used in gyrokinetic code to lighten the numerical cost of simulations, is detailed in subsection 3.3.

3.1. Analytical derivation of the drag term

The quasi-linear operator Q_n (Eq.3) can be written in the form of a Fokker-Planck operator

$$Q_n = \nabla_{\mathbf{v}} \cdot \left[\nabla_{\mathbf{v}} \cdot (\mathbb{D}_n F) - \boldsymbol{\Gamma}_n F \right], \tag{45}$$

where the drag force is defined as

$$\boldsymbol{\Gamma}_n = \nabla_{\mathbf{v}} \cdot \mathbb{D}_n. \tag{46}$$

Eq.45 can be efficiently implemented in a particle-in-cell code by finding the equivalent stochastic process thanks to Ito's lemma. This stochastic process is then discretized using a Euler-Maruyama scheme. More details about this can be found in [11]. In this implementation, it is necessary to compute the drag term Eq.46 which takes the form

$$\boldsymbol{\Gamma}_n = \nabla_{\mathbf{v}} \cdot \mathbb{D}_n = \Gamma_n^{\perp} \hat{\mathbf{e}}_{\perp} + \Gamma_n^{\parallel} \hat{\mathbf{e}}_{\parallel}, \tag{47}$$

with

$$\Gamma_n^{\perp} = \frac{1}{v_\perp} \frac{\partial \left(v_\perp \tilde{D}_n s_n^{\perp} s_n^{\perp} \right)}{\partial v_\perp} + \frac{\partial \left(\tilde{D}_n s_n^{\perp} s_n^{\parallel} \right)}{\partial v_\parallel}, \tag{48}$$

$$\Gamma_n^{\parallel} = \frac{1}{v_\perp} \frac{\partial \left(v_\perp \tilde{D}_n s_n^{\perp} s_n^{\parallel} \right)}{\partial v_\perp} + \frac{\partial \left(\tilde{D}_n s_n^{\parallel} s_n^{\parallel} \right)}{\partial v_\parallel}. \tag{49}$$

The numerical evaluation of the derivatives in velocity space with finite differences is challenging as the resonant diffusion coefficient $\tilde{D}_n$ (Eq.7) displays thin layers in velocity space, especially in the ECCD case. An alternative is to compute analytically the velocity derivatives appearing in Eq.48, 49. Without any simplification, the analytical derivation is challenging and would be numerically expensive. To alleviate this difficulty, some approximations are performed. The first one is to consider the limit of small wavelength as compared to the beam waist size $\sigma \ll 1 \Leftrightarrow \mathcal{N}(\theta_0) W_0 \omega_b \gg c$. For tokamaks with a relatively weak magnetic field, the small wavelength approximation is only marginally valid (i.e. for TCV $W_0 \geq 2$cm, $\omega_b = 82$ GHz, $\mathcal{N}(\theta_0) \sim 1$, $\sigma \lessapprox 0.2$). For devices with stronger magnetic fields, this assumption is legitimately valid (i.e. for ITER $W_0 \geq 2$cm, $\omega_b = 170$ GHz, $\mathcal{N}(\theta_0) \sim 1$, $\sigma \lessapprox 0.1$).

The resonant diffusion coefficient $\tilde{D}_n$, Eq.7, possesses three dependencies with respect to θ_{res}. The first one is in the dispersion relation $\mathcal{N}$, the second in the function $\tilde{\Theta}_k^n$ and the last one in the exponential term $\exp\left[-(\Delta\theta/\sigma)^2\right]$. For $\mathcal{N}$ and $\tilde{\Theta}_k^n$, the difference between the function evaluated at θ_{res} and at θ_0 is proportional to $\Delta\theta \sim \sigma \ll 1$. On the other hand, for the exponential term, one gets $\exp\left[-(\Delta\theta/\sigma)^2\right] - 1 \sim \exp(-1) - 1$ which is a zero order term. Therefore, in the small wavelength limit, at leading order, the resonant diffusion coefficient reads

$$\tilde{D}_{-n}^{\sigma \ll 1} = \frac{\sqrt{\pi} e^2 \mathcal{N}(\theta_0)}{2 m_e^2 \omega_b \sigma} \frac{c}{\left| v_\parallel \right|} \left| E_{\mathbf{0}} \right|^2 \exp\left[-\left(\frac{\Delta\theta}{\sigma} \right)^2 \right] \left| \tilde{\Theta}_{k,0}^n \right|^2, \tag{50}$$

where

$$\tilde{\Theta}_{k,0}^n = \frac{\left[\begin{array}{c} \left[1 + \mathcal{C}_1(\theta_0)\right] J_{n+1}(\tilde{\rho}_0) + \left[1 - \mathcal{C}_1(\theta_0)\right] J_{n-1}(\tilde{\rho}_0) \\ -2\mathcal{C}_2(\theta_0) \frac{v_\parallel}{v_\perp} J_n(\tilde{\rho}_0) \end{array} \right]}{2\sqrt{1 + \mathcal{C}_1(\theta_0)^2 + \mathcal{C}_2(\theta_0)^2}}, \tag{51}$$

with $\tilde{\rho}_0 = \sin(\theta_0)\mathcal{N}(\theta_0)\omega_b v_\perp \gamma/(\Omega_e c)$. The velocity derivatives of the resonant diffusion coefficient in the limit $\sigma \ll 1$ can then be computed

$$\frac{\partial \tilde{D}_{-n}^{\sigma\ll 1}}{\partial v_\perp} = 2\tilde{D}_{-n}^{\sigma\ll 1}\left[\frac{1}{\Theta_{k,0}^n}\frac{\partial \Theta_{k,0}^n}{\partial v_\perp} - \frac{\Delta\theta}{\sigma^2}\frac{\partial \Delta\theta}{\partial v_\perp}\right], \tag{52}$$

$$\frac{\partial \tilde{D}_{-n}^{\sigma\ll 1}}{\partial v_\parallel} = \tilde{D}_{-n}^{\sigma\ll 1}\left[\frac{2}{\Theta_{k,0}^n}\frac{\partial \Theta_{k,0}^n}{\partial v_\parallel} - \frac{1}{v_\parallel} - 2\frac{\Delta\theta}{\sigma^2}\frac{\partial \Delta\theta}{\partial v_\parallel}\right]. \tag{53}$$

The derivatives of $\Theta_{k,0}^n$ with respect to the velocity components are given in the appendix C. The velocity derivatives of $\Delta\theta$ can be computed using

$$\frac{\partial \Delta\theta}{\partial v_{\parallel,\perp}} = -\frac{x_\pm'\left(\lambda^2\right)|\lambda|}{\sqrt{1-x_\pm^2\left(\lambda^2\right)}}\frac{\partial \lambda}{\partial v_{\parallel,\perp}}, \tag{54}$$

where $x_\pm'$ is the derivative of Eq.17, which is straightforward to compute, and the velocity derivatives of λ are given by

$$\frac{\partial \lambda}{\partial v_\parallel} = \frac{n\Omega_e}{c\omega_b}\gamma - \frac{\lambda}{v_\parallel}, \tag{55}$$

$$\frac{\partial \lambda}{\partial v_\perp} = \frac{n\Omega_e}{c\omega_b}\frac{v_\perp}{v_\parallel}\gamma. \tag{56}$$

3.2. Treatment of markers with a low parallel velocity

The drag coefficients diverge for markers with a low parallel velocity. This is due to the fact that the width of the resonant area in the perpendicular velocity direction goes to zero when the parallel velocity goes to zero. Therefore the drag is becoming singular for these low parallel velocities.

To circumvent this issue, markers with a low parallel velocity ($|v_\parallel| < v_{\max}$) are treated differently. For these markers, the distribution function is assumed to be an unshifted Maxwellian F_{Me}. This assumption is motivated by two considerations. First, in absence of a localized source, and even in presence of turbulence, distribution functions of electrons in the core are close to an unshifted Maxwellian. Second, the effective electron-electron collision frequency goes like $\sim (v_T/v)^2$ for $v \ll v_T$ and $\sim (v_T/v)^3$ for $v \gg v_T$, whereas the effective electron-ion collision frequency goes like $\sim (v_T/v)^3$ [15]. For this reason, the low velocity part of the distribution function is often close to a Maxwellian distribution. The assumption that the electron distribution function is an unshifted Maxwellian allows to rewrite the quasi-linear operator Q_n as

$$\begin{aligned} Q_n^M &= \nabla_{\mathbf{v}} \cdot \left[\mathbb{D}_n \cdot \nabla_{\mathbf{v}} F_{Me}\right] \\ &= -\nabla_{\mathbf{v}} \cdot \left[\left(\mathbb{D}_n \cdot \frac{\mathbf{v}}{v_T^2}\right) F_{Me}\right]. \end{aligned} \tag{57}$$

By analogy with Eq.45 we impose for markers with low parallel velocities ($|v_\parallel| < v_{\max}$) the changes $D_n \to 0$ and $\Gamma_n \to \Gamma_n^M$ where

$$\Gamma_n^M = \mathbb{D}_n \cdot \frac{\mathbf{v}}{v_T^2}, \tag{58}$$

where $v_T = \sqrt{T_e/m_e}$ is the thermal velocity of electrons. This simple change of numerical treatment allows avoiding the singularity for low parallel velocities while keeping the same operator (provided that the distribution function is close to a Maxwellian). The choice for $v_{\max}$ is a priori not settled. A numerical study led us to fix the choice of this parameter to $v_{\max} = 0.1 v_T$.

3.3. Usage of an artificial mass ratio between protons and electrons

Gyrokinetic simulations with a real mass ratio between protons and electrons are numerically challenging due to the time and spatial scales separation between the electron and ion dynamics. For this reason, simulations with an artificially reduced mass ratio between protons and electrons are often performed in the gyrokinetic community.

The electron mass appears in the plasma frequency ω_p, in the cyclotron frequency Ω_{ce}, in the prefactor of the resonant diffusion coefficient of Eq.7 and in the definition of the thermal velocity which appears for a term of the form $v_\parallel/c = \left(v_\parallel/v_T\right) \cdot (v_T/c)$ or $v_\perp/c = (v_\perp/v_T) \cdot (v_T/c)$.

In all cases, the real mass of electrons needs to be used in the definitions of the frequencies to ensure the right resonance condition and the proper dispersion relation. One needs to use an artificial speed of light $c^{\text{arti}} = c^{\text{real}}\sqrt{m_e^{\text{real}}/m_e^{\text{arti}}}$ in all terms of the form v_T/c to ensure that $v_T^{\text{arti}}/c^{\text{arti}} = v_T^{\text{real}}/c^{\text{real}}$. Concerning the electron mass appearing in the prefactor of the resonant diffusion coefficient, one needs to use the artificial electron mass. The purpose of this choice is to keep the same normalized diffusion coefficient $\frac{D_n}{v_{T_e}^2\Omega_{ce}} = \frac{D_n m_e^2}{T_e e B}$ between the real and artificial electron masses.

4. Numerical test of ECRH/ECCD source

In this section, testing of the source term described in the previous sections is detailed. In subsection 4.1, an analytical prediction of the minimum and the maximum major radii of absorption is given. The numerical evaluation of the power deposited in the plasma is detailed in subsection 4.2. In subsection 4.3, the evolution of the electron distribution function in the presence of the source term, but without other physical operators, is presented. Finally, subsection 4.4 presents a comparison of ORB5 with the code LUKE when activating all parts of the code, except the turbulence.

4.1. Analytical prediction of the deposition area in real space

The resonant condition $\omega_b = k_\parallel v_\parallel + n\frac{\Omega_e}{\gamma}$ is equivalent to

$$\left(\frac{v_\parallel - \overline{v_\parallel}}{\Delta v_\parallel}\right)^2 + \left(\frac{v_\perp}{\Delta v_\perp}\right)^2 = 1, \tag{59}$$

which is the equation of an ellipse with an average parallel velocity

$$\frac{\overline{v_\parallel}}{c} = \frac{\omega_b k_\parallel c}{\left(k_\parallel c\right)^2 + \left(n\Omega_e\right)^2}, \tag{60}$$

a semi-major axis in the perpendicular direction $\Delta v_\perp$ given by

$$\left(\frac{\Delta v_\perp}{c}\right)^2 = \frac{\left(k_\parallel c\right)^2 + \left(n\Omega_e\right)^2 - \omega_b^2}{\left(k_\parallel c\right)^2 + \left(n\Omega_e\right)^2}, \tag{61}$$

and a semi-minor axis in the parallel direction $\Delta v_\parallel$ given by

$$\left(\frac{\Delta v_\parallel}{c}\right)^2 = \left(\frac{\Delta v_\perp}{c}\right)^2 \frac{\left(n\Omega_e\right)^2}{\left(k_\parallel c\right)^2 + \left(n\Omega_e\right)^2}. \tag{62}$$

By neglecting the poloidal magnetic field, one has $\Omega_e = \Omega_{e,0}\frac{R_0}{R}$, where $\Omega_{e,0} = \frac{eB_0}{m_e}$ is the electron cyclotron frequency on the magnetic axis. Eq.18 implies $k_\parallel R = k_{\parallel,in} R_{in}$. Using these relations allows one to express the characteristics of the ellipse as functions of the major radius R. From these expressions, one can deduce that the resonance between the wave and the plasma is possible only if $R \leq R_{\max}^{\mathrm{res}}$ with

$$R_{\max}^{\mathrm{res}} = \frac{\sqrt{\left(k_{\parallel,in} c R_{in}\right)^2 + \left(n\Omega_{e,0} R_0\right)^2}}{\omega_b}. \tag{63}$$

For all major radii below $R_{\max}^{\mathrm{res}}$ the resonance between the wave and the plasma is a priori possible. But for an efficient coupling between the wave and the plasma, particles fulfilling the resonance condition Eq.59 are needed. If one assumes the distribution function of electrons to be an unshifted Maxwellian of temperature T_e, a reasonable coupling between the wave and the electrons is possible only if

$$-3v_T^{\mathrm{res}} \leq \left|\overline{v_\parallel}\right| - \Delta v_\parallel \leq 3v_T^{\mathrm{res}} \tag{64}$$

where v_T^{res} is the thermal velocity of electrons at the position of maximum absorption. As $\left|\overline{v_\parallel}\right| - \Delta v_\parallel$ is an increasing function of the major radius, the condition Eq.64 allows determining a minimal major radius $R_{\min}^{\mathrm{eff}}$ and maximal major radius $R_{\max}^{\mathrm{eff}}$ for an efficient absorption, which read

$$R_{\max/\min}^{\mathrm{eff}} = \frac{\pm 3v_T^{\mathrm{res}}\left|k_{\parallel,in}\right| R_{in} + n\Omega_{e,0} R_0 \sqrt{1 - \left(3\frac{v_T^{\mathrm{res}}}{c}\right)^2}}{\omega_b}. \tag{65}$$

Note that the computation of $R_{\min}^{\mathrm{eff}}$ and $R_{\max}^{\mathrm{eff}}$ is valid only for an unshifted Maxwellian. For a shifted Maxwellian, or a distribution function with a non negligible deviation to a Maxwellian, the absorption boundaries can be shifted. For most of the numerical tests presented in this article, unshifted Maxwellians are a good proxy of the actual distribution function. Note that this is no longer true for the cases with a high power deposition as presented in subsection 4.4. Furthermore, it is noteworthy that the inner bound $R_{\min}^{\mathrm{eff}}$ is a theoretical limit for efficient absorption of the beam. For cases with large density and temperature, most of the beam power is absorbed before reaching this inner major radius.

4.2. Computation of the power deposition

The source is numerically implemented in ORB5 [12] via a Langevin equation as in [11]. The power deposited on a given marker i reads

$$\begin{aligned}\frac{\left\langle \Delta\left(v_i^2\right)\right\rangle}{\Delta t} &= 2\sum_n \left[v_{\parallel,i}\Gamma_{n,i}^{\parallel} + v_{\perp,i}\Gamma_{n,i}^{\perp} + D_{n,i}\left[\left(s_{n,i}^{\parallel}\right)^2 + \left(s_{n,i}^{\perp}\right)^2\right]\right] \\ &+ \Delta t \sum_n \left[\left(\Gamma_{n,i}^{\parallel}\right)^2 + \left(\Gamma_{n,i}^{\perp}\right)^2\right],\end{aligned} \tag{66}$$

where the brackets $\langle . \rangle$ stand for the ensemble average. By multiplying this quantity by the weight of the marker times $m_e/2$, and by summing over the markers in a spatial bin, one gains access to the ensemble average power deposition on this bin. Note that Eq.66 allows putting a quantitative limit on the maximum time step which is allowed for a given source amplitude, as the term proportional to Δt in Eq.66 should always be small compared with the term independent of the time step.

4.3. Test with only the source

In this section the electron distribution function is evolved only by the source operator $dF_e/dt = Q_n$, where Q_n is the quasi-linear operator described above in Eq.3. In all the tests presented in this section and the next one, a beam with an X polarization and interacting with the second harmonic of the cyclotron frequency ('X2' in short) is simulated and an analytical axisymmetric magnetic geometry with $\mathbf{B} = \frac{B_0 R_0}{R}\left[\frac{\epsilon}{\bar{q}}\mathbf{e}_\chi + \mathbf{e}_\varphi\right]$ is used. In this expression, χ is the poloidal angle, φ is the toroidal angle, $\epsilon = r/R_0$ is the inverse aspect ratio and $\bar{q} = q\sqrt{1-\epsilon^2}$, where q is the safety factor. In all the tests presented in this section and the next one, typical TCV values have been used ($B_0 = 1.4$ T, $R_0 = 0.89$ m, $a = 0.25$ m).

In this subsection only, to simplify the test of the source, the safety factor $q = 10$ is constant and the plasma density N_e and temperature T_e are chosen to have no spatial dependence. The density and temperature are scanned around reference values $N_e^{\mathrm{ref}} = 2{\cdot}10^{18}\ \mathrm{m}^{-3}$, $T_e^{\mathrm{ref}} = 1.17\,\mathrm{keV}$, to test the source behavior. The reference density has been chosen quite low to have approximately half the power absorbed. This case is the most stringent test for the model. Indeed, with a larger density, the beam would be fully absorbed and the sensitivity to the numerical parameters would be weaker than in the case of half absorption. On the other hand, a really weak absorption would not numerically test the model of absorption described in section 2.4.

The frequency of the beam $f_{\mathrm{beam}} = 78$ GHz is chosen to have the maximum of absorption near the magnetic axis. It allows one to simulate only a restricted volume of the plasma $r < 0.2a$ and so to have a large density of markers with a limited cost for the simulation. For the results shown in Figs.2, 3 and 4, $N_p = 2 \cdot 10^8$ markers were used. With this choice, the simulation results are numerically converged as discussed in Fig.5. The power of the beam is chosen to be small enough so that the distribution function stays close to a Maxwellian, allowing a direct comparison between ORB5 results and Albajar's prediction, which assumes a Maxwellian distribution for electrons.

The profiles of absorption for a pure ECRH and a mixed ECRH/ECCD for the reference density and temperature are shown in Fig.2. In both cases, excellent agreement is found between the numerical results obtained with ORB5 and the analytical prediction [13]. Furthermore, the absorption is taking place between the minimum $R_{\mathrm{min}}^{\mathrm{th}}$ and the maximum $R_{\mathrm{max}}^{\mathrm{th}}$ major radii computed in subsection 4.1. The agreement between ORB5 and the theoretical prediction is maintained for a different density Fig.3 or temperature Fig.4, validating the derivation of the model and its implementation in ORB5.

A convergence test is performed in Fig.5. Fast convergence is obtained both in a pure ECRH and a mixed ECRH/ECCD case. More markers are needed to converge in the pure ECRH case as the deposition is narrower in real space, but, in both cases, a good quantitative agreement with the analytical prediction is found, even with a low resolution (which would be under-resolved for a simulation in the presence of turbulence).

4.4. Benchmark against drift-kinetic simulations

In this section, the code ORB5 is compared with the code LUKE, which is a 3D relativistic bounce-average drift-kinetic Fokker-Planck solver for the electron distribution function $F_e(\rho, v_\parallel, v_\perp)$ [16], coupled to the ray-tracing code C3PO [14], and

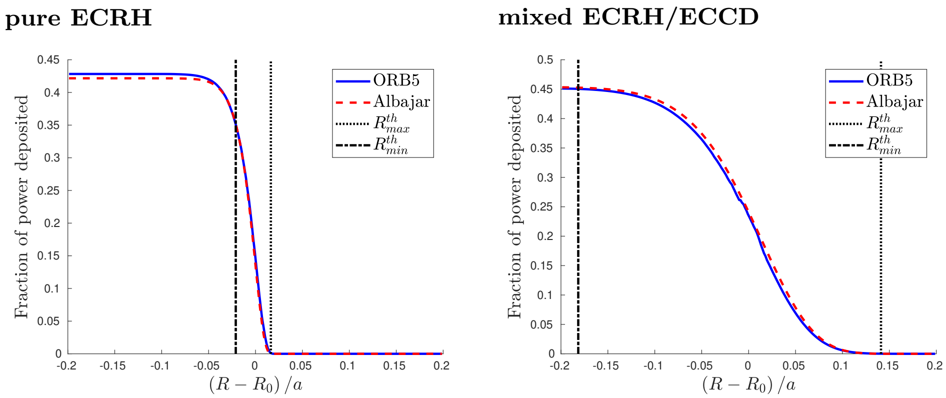

Figure 2. Fraction of power absorbed as a function of the major radius for a pure ECRH case ($\theta_{in} = 0.5\pi$) on the left and a mixed case ECRH/ECCD ($\theta_{in} = 0.4\pi$) on the right. The electron density $N_e = 2 \cdot 10^{18} m^{-3}$ and temperature $T_e = 1.17\ keV$ are constant.

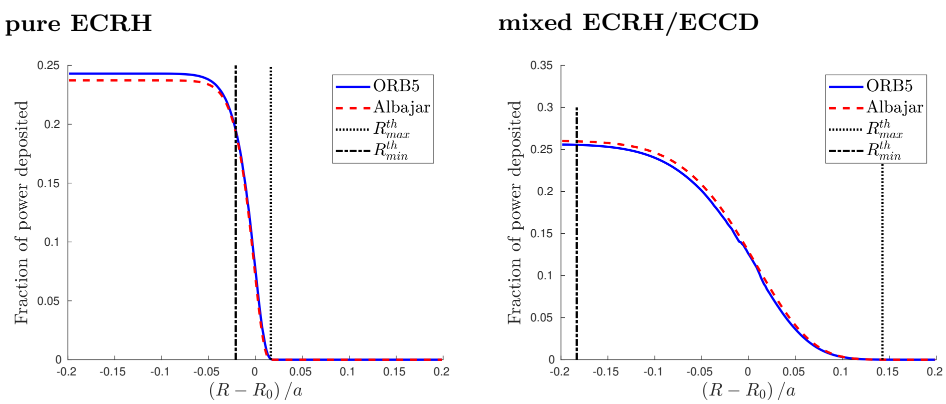

Figure 3. Same as Fig.2 except for the density $N_e = 10^{18} m^{-3}$.

is mainly used to study suprathermal electron physics, especially Electron-Cyclotron and Lower-Hybrid current-drive problems. Physics operators included in LUKE are collision, Ohmic electric field, quasilinear wave-plasma interaction and additional ad-hoc radial transport of fast electrons, in the form of bounce-average Fokker-Planck operators. The basis of the quasilinear treatment of the wave-plasma interaction is similar in LUKE and ORB5 [11].

In this subsection, all parts of the ORB5 code are activated (source, collisions, Vlasov and quasi-neutrality). The non axisymmetric modes of the electric potential are filtered out at each time step to remove the turbulence as LUKE cannot simulate it. As a consequence, the ad-hoc radial transport of fast electrons is not activated

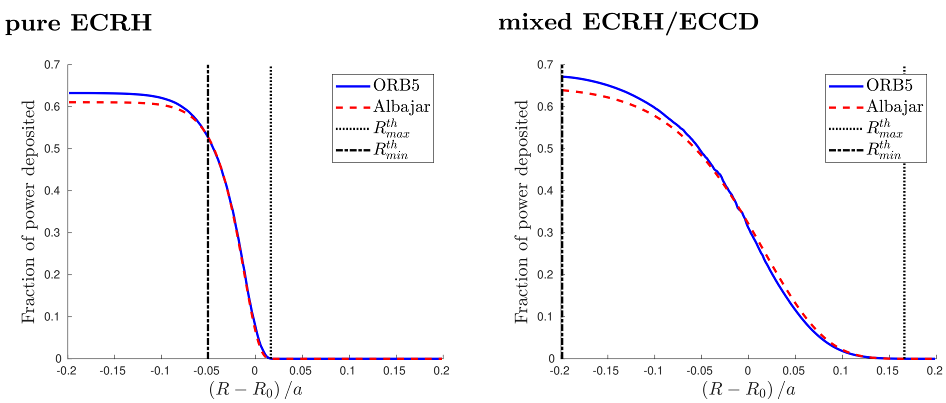

Figure 4. Same as Fig.2 except for the temperature $T_e = 2.08\ keV$.

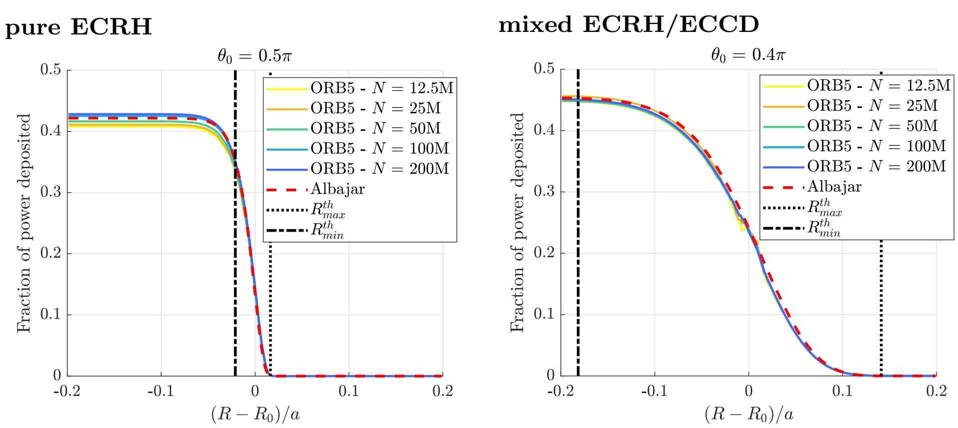

Figure 5. Convergence test for a pure ECRH case ($\theta_{in} = 0.5\pi$) on the left and a mixed ECRH/ECCD case ($\theta_{in} = 0.4\pi$) on the right. The electron density $N_e = 2 \cdot 10^{18} m^{-3}$ and temperature $T_e = 1.17\ keV$ are constant.

in LUKE, as it is supposed to model turbulent transport. Within this framework, both codes solve similar problems. Some differences remain between the two codes. Firstly, LUKE solves a bounce-average problem whereas ORB5 solves the 5D problem. The collision operators are also different as ORB5 possesses a nonlinear collision operator, but without relativistic corrections [17], whereas LUKE uses a linearized collision operator with a relativistic model for electron-electron collisions [18], and non-relativistic Maxwellian ion background model for electron-ion collisions, as described in [19]. Ion-ion collisions are not treated in LUKE, as ions are not simulated and a Maxwellian distribution is assumed for their distribution. Finally, the computation of the power along the beam is different between the two models. Indeed, ORB5 uses Albajar's linear model to compute the local power of the beam and therefore disregards some quasi-linear effects. On the other hand, the calculation scheme of LUKE/C3PO, detailed in [16], retains all quasi-linear effects. In LUKE, a first guess of the linear power deposited by the EC waves is found by the ray-tracing, assuming a Maxwellian background plasma. The total wave power is carried by a total of 24 independent rays, and the different ray contributions are integrated together over real and velocity space. Then, the associated diffusion coefficient is evaluated and used in the Fokker-Planck solver to find the new distribution function. The deposited power is re-evaluated, and ray power content is corrected by wave power balance so that a new diffusion coefficient is found. A convergence loop is made such that the calculations of the absorbed power density using the diffusion coefficient and the electron distribution function are consistent with a relative accuracy of $\leq 1\%$, dealing with the quasilinear nature of the absorbed power (interdependence of absorbed power and distribution function).

The chosen equilibrium for the benchmark is an analytic TCV-like equilibrium generated with the method explained in the appendix of [20], with minor radius $a = 0.25$ m, major radius $R_0 = 0.89$ m, magnetic field on axis $B_0 = 1.4$ T, a parabolic safety factor profile $q(r = R - R_0) = q_0 + (q_a - q_0)(r/a)^2$ (with $q_0 = 1$ and $q_a = 3$), constant density N_e^{ref} and a temperature profile corresponding to realistic temperature profiles obtained in TCV, as described in [21]

$$\frac{T_e(\rho_P)}{T_{\mathrm{edge}}} = \begin{cases} \bar{T}_{\mathrm{axis}} + \lambda_T \rho_P^2 & \text{if} \quad \rho_P \leq \rho_{P,1} \\ \bar{T}_{\mathrm{ped}} \exp\left[-\kappa_T(\rho_P - \rho_{P,2})\right] & \text{if} \quad \rho_{P,1} \leq \rho_P \leq \rho_{P,2} \\ 1 - \mu_T(\rho_P - \rho_{P,3}) & \text{if} \quad \rho_{P,2} \leq \rho_P \leq \rho_{P,3} \\ 1 & \text{if} \quad \rho_P \geq \rho_{P,3} \end{cases} \tag{67}$$

where $\rho_P = \sqrt{\psi_P/\psi_{P,a}}$ (and ψ_P is the poloidal magnetic flux), $\rho_{P,1} = 0.27$, $\rho_{P,2} = 0.72$, $\rho_{P,3} = 0.90$ and

$$\begin{cases} \bar{T}_{\mathrm{axis}} &= \bar{T}_{\mathrm{core}} - \lambda_T \rho_{P,1}^2 \\ \bar{T}_{\mathrm{core}} &= \bar{T}_{\mathrm{ped}} \exp\left(-\kappa_T(\rho_{P,1} - \rho_{P,2})\right) \\ \bar{T}_{\mathrm{ped}} &= 1 - \mu_T(\rho_{P,2} - \rho_{P,3}) \end{cases} \tag{68}$$

with $\lambda_T = -\kappa_T \bar{T}_{\mathrm{core}}/(2\rho_{P,1})$, $\kappa_T = 3$, $\mu_T = 12$ and $T_{\mathrm{edge}} = 140$ eV. A pure hydrogen plasma is assumed with $N_e = N_i$ and $T_e = T_i$, and no Ohmic electric field is considered (this option is not available in ORB5). In that case, the system is invariant by the change of coordinates $v_\parallel \to -v_\parallel$ and $\theta_0 \to \pi - \theta_0$. Then, for the energy absorption, there is no difference between $\theta_0 \leq \pi/2$ and $\theta_0 \geq \pi/2$.

For all ORB5 simulations, $2 \cdot 10^8$ and 10^9 markers have been used for representing the ions and electrons respectively. With these resolutions, the results are converged with respect to the number of markers. In LUKE, the size of the phase space grid $(p, \xi = p_\parallel/p, \rho)$ is $151 \times 121 \times 30$. The points in the spatial grid are not linearly spaced, they are concentrated around the power absorption location, guessed from the linear ray-tracing calculation.

ORB5 simulations have been performed using two different proton-electron mass ratios ($m_i/m_e = 100$ or 1836). The advantage of using an artificially reduced mass ratio is to increase the time step of the simulation ($\Delta t = 1.0\ \Omega_{ci}^{-1}$ for the simulations with $m_i/m_e = 100$ and $\Delta t = 0.1\ \Omega_{ci}^{-1}$ for the simulations with $m_i/m_e = 1836$), leading to lighter numerical cost. In order to have the collision physics as close as possible between the two types of simulations, a modification of the collisionality is applied for the simulations with the artificial mass ratio. Indeed, the collision frequency of a species a on a species b reads [17]

$$\nu_{ab} = \frac{\ln\Lambda}{3\pi^{3/2}\epsilon_0^2}\frac{N_b}{T_a^{3/2}}\frac{e_a^2 e_b^2}{\sqrt{m_a}}\frac{\left(1+\frac{m_a}{m_b}\right)}{\left[1+\frac{m_a T_b}{m_b T_a}\right]^{3/2}}. \tag{69}$$

By considering the fact that electrons are much lighter than ions, one can see that the electron-electron ν_{ee} and electron-ion ν_{ei} collision frequencies are proportional to $m_e^{-1/2}$. For simulations with heavy electrons, the correct ratio between the collision frequency of electrons and the electron cyclotron frequency, which is the most relevant dimensionless parameter to study the impact of the source in the presence of collisions, can be retrieved by simply multiplying the collision frequency of reference in ORB5 by $\sqrt{m_e^{\mathrm{real}}/m_e^{\mathrm{arti}}}$. This choice is made to retain the correct physics as much as possible when using an artificial mass ratio between protons and electrons. Note that, with this choice, the electron collisionality $\nu_e^\star = \frac{(\nu_{ee}+\nu_{ei})qR}{\epsilon v_{Te}}$ is lower than the real one. This choice therefore lowers the neoclassical transport of electrons. Furthermore, this hypothesis could have an impact in the presence of trapped electron mode turbulence, which is sensitive to the electron collisionality.

The two angles of injection $\theta_{0,in}$ used in the benchmark are illustrated in figure 6, which shows C3PO ray-tracing results (poloidal and top views) for equatorial propagation of the beam. In the pure ECRH case ($\theta_{0,in} = 0.5\pi$) the ray goes straight in the plasma as expected, whereas for the case with an ECCD component ($\theta_{0,in} = 0.4\pi$), the beam is slightly curved, accordingly to predictions in the subsection 2.2. Comparisons between ORB5 and LUKE/C3PO for the two angles of injection and for two different densities ($N_e^{\mathrm{ref}} = 5\cdot 10^{18}\ \mathrm{m}^{-3}$ and $N_e^{\mathrm{ref}} = 1\cdot 10^{19}\ \mathrm{m}^{-3}$) are shown in figures 7, 8, 9 and 10. In each of these plots, the linear predictions of Albajar and C3PO are given as reference points. Error bars on LUKE absorbed power come from the relative gap on absorbed power density between the last iteration and the one before (basically less than 1% for completely converged simulations). In LUKE, error bars on the Full-Width at Half Maximum (FWHM) of the deposition profile and on absorption location come from the spatial grid resolution. In ORB5, error bars on all quantities correspond to the standard deviation with respect to time.

At low power, an excellent agreement is found between all the predictions for the pure ECRH cases Fig.7, 9. The agreement for the ECCD cases Fig.8, 10 at low power is still good, but a mismatch of approximately 10% is found for the total power absorbed predicted by ORB5 compared with the other predictions. As the total power absorbed is not constrained in the model implemented in ORB5, the fact that the total power absorbed is above 100% is not a problem. If this point becomes critical for later applications of this source term, a convergence loop between the energy deposited on the distribution function and the one included in the ray could be implemented in a similar way as the one used in LUKE. This possibility has not been added in ORB5 yet, as it would significantly increase the numerical cost of the source term. The overall agreement at low power for all cases validates the implementation of the model in ORB5.

For high-power beams, quasi-linear effects become important, especially for the total absorbed power. For the pure ECRH cases Fig.7, 9, quasi-linear effects lead to a significant decrease of the total power deposited both in LUKE and ORB5. These quasi-linear effects are stronger for LUKE than for ORB5. The quantitative difference between the results from the two codes can come from the fundamental differences

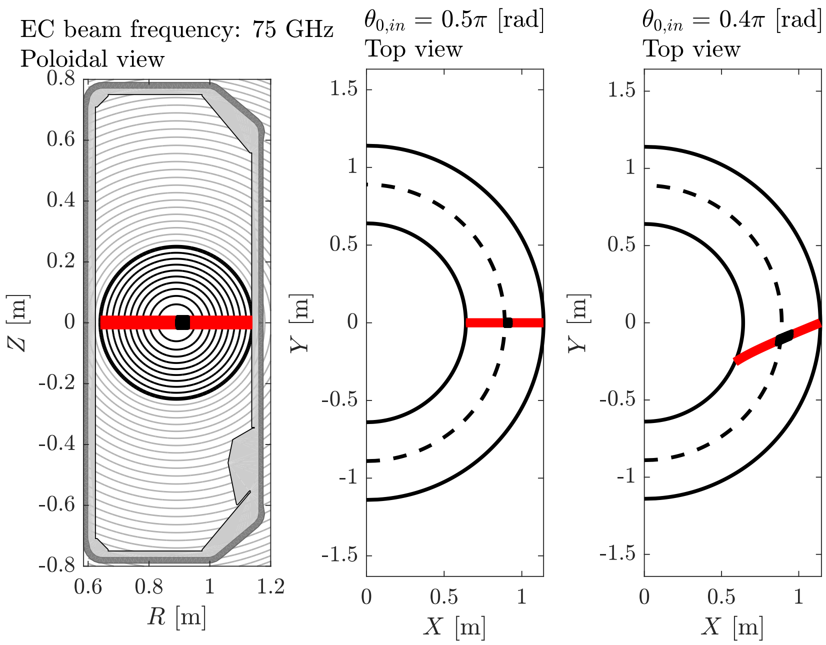

Figure 6. Results of C3PO ray tracing for equatorial midplane ECCD, launched from the Low Field Side, with an EC beam frequency of 75 GHz, and the angle $\theta_{0,in}$ between the beam wave vector $\mathbf{k}$ and the magnetic field $\mathbf{B}$ at the beam entrance in the plasma ranging from $\pi/2$ (pure ECRH) to 0.4π.

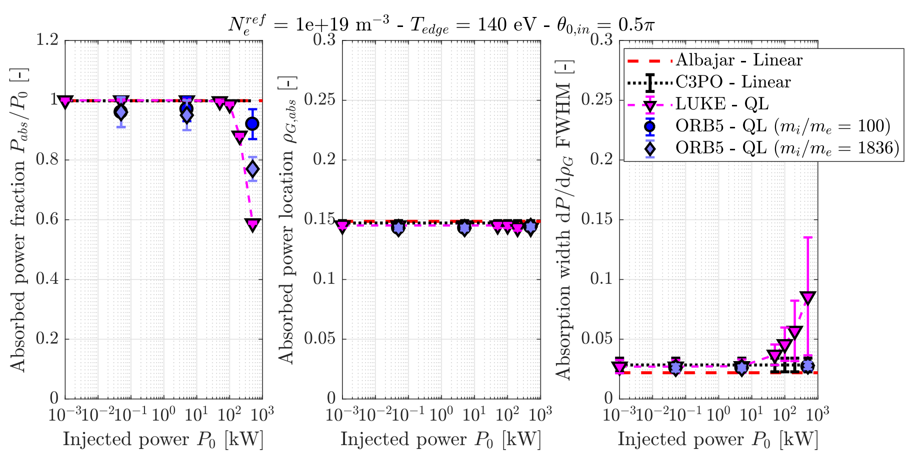

Figure 7. Results of injected power P_0 scan, for $\theta_{0,in} = \pi/2$, for Albajar's theoretical prediction, C3PO (linear calculation), quasilinear LUKE, and ORB5, showing total absorbed power fraction (*left*), power absorption location $\rho_{G,abs}$ (*right*) and full width at half maximum $(\Delta\rho_G)_{abs}$ of the power deposition profile dP_{abs}/dρ_G, where $\rho_G = (R - R_0)/a$, (*center*).

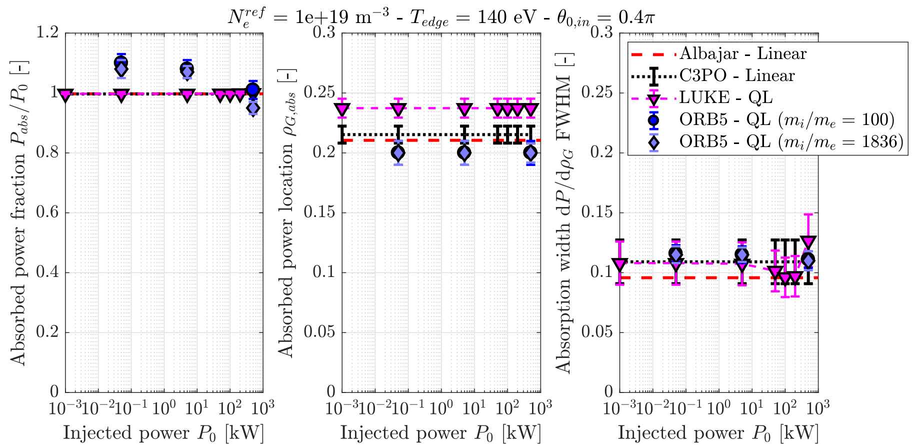

Figure 8. Results of injected power P_0 scan, for $\theta_{0,in} = 0.4\pi$, for Albajar's theoretical prediction, C3PO (linear calculation), quasilinear LUKE, and ORB5, showing total absorbed power fraction (*left*), power absorption location $\rho_{G,abs}$ (*right*) and full width at half maximum $(\Delta\rho_G)_{abs}$ of the power deposition profile $\mathrm{d}P_{abs}/\mathrm{d}\rho_G$, where $\rho_G = (R - R_0)/a$, (*center*).

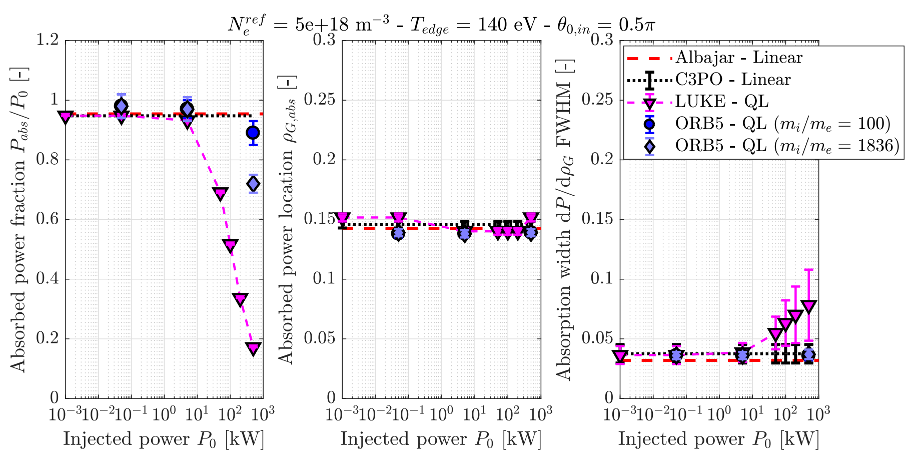

Figure 9. Results of injected power P_0 scan, for $\theta_{0,in} = 0.5\pi$ at lower density ($N_e^{\mathrm{ref}} = 5 \cdot 10^{18}$ m^{-3}), for Albajar's theoretical prediction, C3PO (linear calculation), quasilinear LUKE, and ORB5, showing total absorbed power fraction (*left*), power absorption location $\rho_{G,abs}$ (*right*) and full width at half maximum $(\Delta\rho_G)_{abs}$ of the power deposition profile $\mathrm{d}P_{abs}/\mathrm{d}\rho_G$, where $\rho_G = (R - R_0)/a$, (*center*).

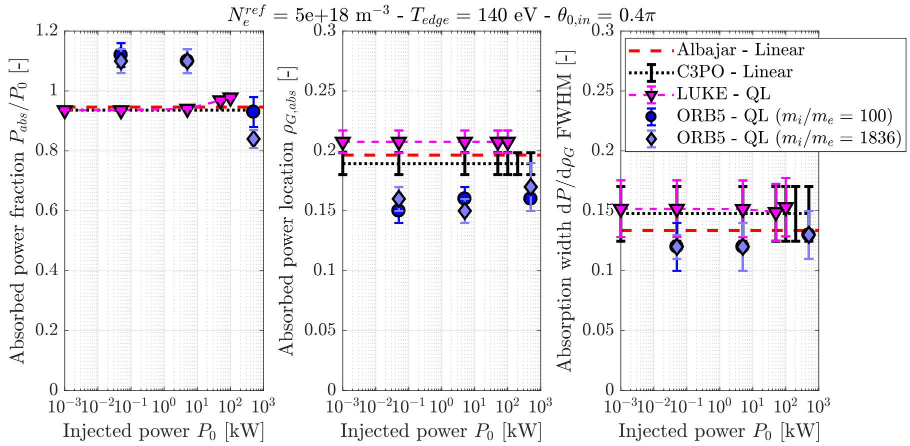

Figure 10. Results of injected power P_0 scan, for $\theta_{0,in} = 0.4\pi$ at lower density ($N_e^{\mathrm{ref}} = 5 \cdot 10^{18}$ m^{-3}), for Albajar's theoretical prediction, C3PO (linear calculation), quasilinear LUKE, and ORB5, showing total absorbed power fraction (*left*), power absorption location $\rho_{G,abs}$ (*right*) and full width at half maximum $(\Delta\rho_G)_{abs}$ of the power deposition profile $\mathrm{d}P_{abs}/\mathrm{d}\rho_G$, where $\rho_G = (R - R_0)/a$, (*center*).

between the two codes, i.e. 3D bounce-average for LUKE compared with 5D drift-kinetic for ORB5, but also from the difference between the collision operators (linear with relativistic correction for LUKE, nonlinear but without relativistic correction for ORB5), or the feedback loop on the power absorbed by the plasma and the power of the beam, which is included in LUKE but not in ORB5. It is also noteworthy that ORB5 simulations using the real mass ratio between electrons and protons display larger quasi-linear effects than the one using heavy electrons. This difference is probably due to the difference in collisionality between the two versions of the code. It implies that simulations using the true electron mass will have to be used for the simulations dedicated to the study of quasi-linear effects. Simulations with a non zero current drive component, Fig.8, 10, display smaller quasi-linear effects in both codes.

Quasilinear dependencies at high injected power can be interpreted by writing the equation for the deposited power density in the momentum-pitch-angle coordinates $(p, \xi = p_{\|}/p)$

$$\frac{\partial P}{\partial V} = mc^2 \int_0^{\infty} \mathrm{d}p(\gamma - 1) \int_{-1}^{1} \left[\frac{1}{p^2} \frac{\partial}{\partial p} \left(p^2 S_p \right) - \frac{1}{p} \frac{\partial}{\partial \xi} \left(\sqrt{1 - \xi^2} S_\xi \right) \right] \mathrm{d}\xi, \tag{70}$$

where the flux $\mathbf{S}$ in (p, ξ) is given by

$$\mathbf{S} = -\mathbb{D}_n \cdot \nabla_{\mathbf{p}} F_e = \begin{pmatrix} S_p \\ S_\xi \end{pmatrix} = \begin{pmatrix} -D_{pp} \frac{\partial F_e}{\partial p} + \frac{\sqrt{1-\xi^2}}{p} D_{p\xi} \frac{\partial F_e}{\partial \xi} \\ -D_{\xi p} \frac{\partial F_e}{\partial p} + \frac{\sqrt{1-\xi^2}}{p} D_{\xi\xi} \frac{\partial F_e}{\partial \xi} \end{pmatrix}, \tag{71}$$

with $\mathbb{D}_n$ the diffusion tensor resulting from wave-particle interaction, as defined in [11], and D_{pp}, $D_{p\xi}$, $D_{\xi p}$ and $D_{\xi\xi}$ its components in (p, ξ) coordinates. The dominant diffusion term is D_{pp} (at least by an order of magnitude in all cases considered in this paper), so the quasilinear behavior can be partly understood by looking at the product $D_{pp} \frac{\partial F_e}{\partial p}$ at the absorption location in phase space. The quasilinear evolution of the total absorbed power results from a balance between the relative evolution of

D_{pp} with injected power due to the modification of the beam power along its path (quasilinear effect due to the loop between the energy deposited on the plasma and the power carried by the beam, which is not included in ORB5) and the deviation of F_e from a Maxwellian, resulting from the competition between the source, collisions and the neoclassical physics (turbulence is not inluded in these simulations).

In the pure ECRH case, the flattening of the distribution by the source, illustrated on Fig.11 is the dominant effect and leads to a drop of the fraction of power absorbed as seen in Fig.7 and 9. The flattening of the distribution function increase with the absorbed power, explaining the dependence of quasi-linear effects with respect to the injected power seen on Fig.7 and 9. On the opposite, an increase of the collisionality, for instance by increasing the density, reduces the deviations from the Maxwellian and explains the difference of quasilinear effects between Fig.7 and 9 at large power.

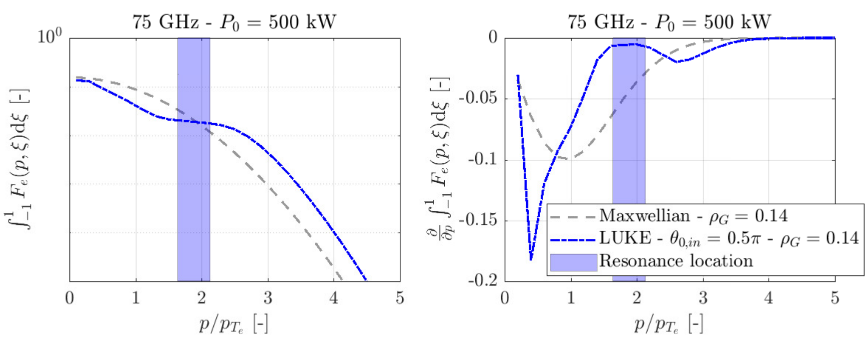

Figure 11. Pitch-angle integrated distribution function of electrons obtained with LUKE (*left*) and its derivative with respect to p (*right*), for the pure ECRH, at the maximum of absorption $\rho_{G,abs}$, compared with the initial Maxwellian distribution. The distribution function is obtained for the high injected power case. The shaded area shows a rough approximation of the resonance location. The flattening of the distribution function leads to a decrease of the local power deposited by ECRH

For the case with ECCD, represented in Fig.8 and 10, the combined effect of the source and the collision pitch-angle scattering can result in a large pitch-angle-dependent population of suprathermal electrons, illustrated in Fig.12, which shows the electron distribution in (p, ξ) space at the absorption location. The presence of a suprathermal population increases the power absorbed. In the case of ECCD, the two mechanisms described above, i.e. flattening of the distribution function by the source which leads to a reduction of the absorbed power on the one hand, and the increase of the suprathermal population by the combination of the source and collisions leading to an increase of the absorbed power on the other hand, are in direct competition. The overall effect is therefore case dependent and sensitive to the collision operator. This explains the difference between ORB5, which predicts a decrease of the power in the ECCD case studied here, and LUKE, which predicts a small increase of the absorbed power as can be seen in Fig.8 and 10.

The combination of low density, high temperature and high power leads to difficulty in convergence of the quasilinear power deposition in LUKE, as the collision frequency is low and the quasilinear diffusion is high. This translates the fact that the power density becomes high, leading to strong quasilinear distortions of the distribution, with less collisions to fill the hole the wave dug in the distribution. LUKE simulations convergence is ensured in figures 7, 8 and 9, but it could not be reached for $P_0 > 100$ kW at lower density in ECCD ($N_e^{\mathrm{ref}} = 5 \cdot 10^{18}$ m^{-3}, Fig. 10).

The quantitative agreement between ORB5 and LUKE for low power deposition and the qualitative agreement at high power validate the derivation of the source term and its implementation in ORB5. The ORB5 code is therefore ready to study the turbulence in the presence of the ECRH/CD source. This study is left for a future paper.

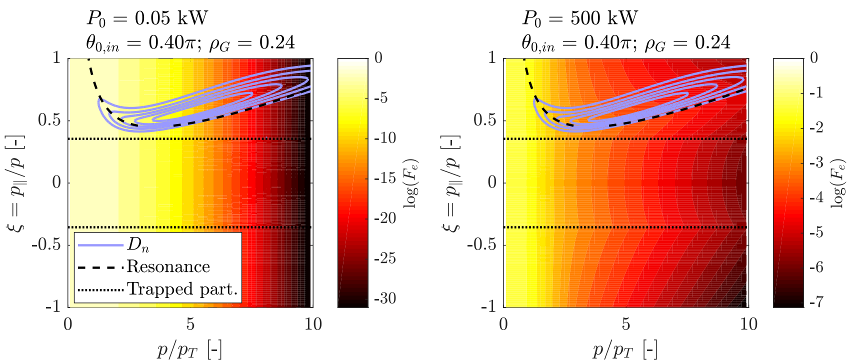

Figure 12. 2-D distribution function of electron obtained with LUKE, at maximum of absorption $\rho_{G,abs}$ for each angle, for high injected power. The dominant term of the RF quasilinear bounce-averaged diffusion coefficient D_{pp} is overlaid, as well as a theoretical prediction for the resonance location (see [22]). In ECCD, the resonance is pitch-angle dependent, leading to wave interaction with particles at higher p. At low power, the distribution remains close to Maxwellian.

5. Conclusion

In this paper, a quasilinear operator representing the electron cyclotron resonance heating and current drive is derived in the specific case of a beam propagating in the equatorial plane of an axisymmetric tokamak. This assumption allows one to treat the beam propagation in the plasma analytically, removing the need for the coupling with a dedicated beam propagation code, such as a ray- or beam-tracing code.

This operator can be used as a source term in any global gyrokinetic code. It has been implemented in the particle-in-cell code ORB5. The numerical treatment specific to particle-in-cell code is detailed. The numerical implementation is validated against an analytical model for the linear absorption. The quasilinear corrections are also tested by benchmarking ORB5 against the bounce-average drift-kinetic code LUKE, which is dedicated to the simulation of the electron distribution function in the presence of plasma/wave interactions. A good agreement is found between the two codes despite some differences in the limit of large power deposition, which are discussed in detail. A further development of the model may include the implementation of a convergence loop on the deposited power (as it is done in LUKE), but this will dramatically increase the cost of already heavy simulations, especially if a realistic electron-to-ion mass ratio is required.

The implementation of the source term described in this paper in any global gyrokinetic code enables the self-consistent study of turbulence in presence of ECRH/ECCD by this code. The next step of this project is to study the interplay between this realistic source of momentum and energy on the one hand, and the turbulence on the other hand. This study will help to elucidate a long standing question about the possibility for turbulence to radially transport suprathermal electrons generated by the resonant wave/particle interaction outside the resonant area, a mechanism has been proposed to reconcile theoretical predictions with experimental observations made in some cases [1, 2].

Acknowledgment

This work was supported by a grant from the Swiss National Supercomputing Centre (CSCS) under project s1067. Some of the simulations presented here were obtained on the EUROfusion partition of the MARCONI100 supercomputer. This work was supported in part by the Swiss National Science Foundation. This work has been carried out within the framework of the EUROfusion Consortium, funded by the European Union via the Euratom Research and Training Programme (Grant Agreement No 101052200 — EUROfusion). Views and opinions expressed are however those of the author(s) only and do not necessarily reflect those of the European Union or the European Commission. Neither the European Union nor the European Commission can be held responsible for them.

Appendix A: Group velocity for an oblique propagation

For the evaluation of Eq.27, it is necessary to compute the group velocity in the general case. It can be shown that the group velocity is given by

$$\left|v_{g,O/X}\right| = \frac{c\mathcal{N}_{O/X}}{\mathcal{N}^2_{O/X} + \frac{\omega_b}{2}\frac{\partial \mathcal{N}^2_{O/X}}{\partial \omega_b}} \tag{72}$$

The cold plasma dispersion relation Eq.12 can be written differently

$$\mathcal{N}^2_{O/X} = \frac{f_1\left(\omega_b^2\right) \pm \frac{\Omega_e \omega_p^2}{\omega_b}\sqrt{f_2\left(\omega_b^2\right)}}{f_3\left(\omega_b^2\right)} \tag{73}$$

where

$$f_1(x) = 2\left(\tan^2\theta + 1\right)\left[\left(x - \omega_p^2\right)^2 - x\Omega_e^2\right] + \left(\tan^2\theta + 2\right)\omega_p^2\Omega_e^2 \tag{74}$$

$$f_2(x) = \Omega_e^2 \tan^4\theta x + 4\left(x - \omega_p^2\right)^2\left(\tan^2\theta + 1\right) \tag{75}$$

$$f_3(x) = 2\left[\left(x - \omega_p^2 - \Omega_e^2\right)x\left(\tan^2\theta + 1\right) + \omega_p^2\Omega_e^2\right] \tag{76}$$

This formulation allows one to express the group velocity as

$$\left|v_{g,O/X}\right| = \frac{c\mathcal{N}_{O/X} f_3\left(\omega_b^2\right)}{g_1\left(\omega_b^2\right) \pm \frac{\Omega_e\omega_p^2}{2\omega_b}\frac{g_2\left(\omega_b^2\right)}{\sqrt{f_2\left(\omega_b^2\right)}} - \mathcal{N}^2_{O/X} g_3} \tag{77}$$

where

$$g_1(x) = x f_1'(x) = 2\left(\tan^2\theta + 1\right)x\left[2\left(x - \omega_p^2\right) - \Omega_e^2\right] \tag{78}$$

$$g_2(x) = x f_2'(x) - f_2(x) = 4\left(\tan^2\theta + 1\right)\left(x^2 - \omega_p^4\right) \tag{79}$$

$$g_3(x) = x f_3'(x) - f_3(x) = 2\left[\left(\tan^2\theta + 1\right)x^2 - \omega_p^2\Omega_e^2\right] \tag{80}$$

The analytical expression of the group velocity Eq.77 can be used for an efficient implementation linking the electric field of the beam to its power Eq.27

Appendix B: Evaluation of the Bessel functions and their derivatives for the theoretical prediction

In this section, the function $\frac{\left|J_{m+1/2}(z_n)\right|^2}{x_n}$ where $z_n = \frac{1}{2}\left(\sqrt{4x_n^2 - y_n^2} + iy_n\right)$ is derived with respect to x_n and y_n. These derivatives are useful to evaluate Eq.33 in the theoretical prediction.

Case $\Re\left(z_n\right) > 0$

When $\Re\left(z_n\right) > 0$, i.e. when $4x_n^2 > y_n^2$, one can use the spherical Bessel function of first kind j_m which is related to $J_{m+\frac{1}{2}}$ via the relation (Eq. 10.1.1 of [23])

$$J_{m+\frac{1}{2}}\left(z\right) = \sqrt{\frac{2z}{\pi}} j_m\left(z\right) \tag{81}$$

which is valid for any integer m and any complex argument z. In practice, only the low m integer are useful. One can then use the fact that (Eq.10.1.10 of [23])

$$j_m\left(z\right) = f_m\left(z\right)\sin\left(z\right) + \left(-1\right)^{m+1} f_{-m-1}\left(z\right)\cos\left(z\right) \tag{82}$$

where $f_0\left(z\right) = z^{-1}$, $f_1\left(z\right) = z^{-2}$ and (Eq. 10.1.19 of [23])

$$f_{m-1}\left(z\right) + f_{m+1}\left(z\right) = \left(2m+1\right) f_m\left(z\right)/z. \tag{83}$$

The first values of $f_m\left(z\right)$ are given in Tab 1.

m	$f_m\left(z\right)$	m	$f_m\left(z\right)$
-5	$105z^{-4} - 10z^{-2}$	0	z^{-1}
-4	$-15z^{-3} + z^{-1}$	1	z^{-2}
-3	$3z^{-2}$	2	$3z^{-3} - z^{-1}$
-2	$-z^{-1}$	3	$15z^{-4} - 6z^{-2}$
-1	0	4	$105z^{-5} - 45z^{-3} + z^{-1}$

Table 1. Values of $f_m\left(z\right)$ for low m integers

Using the fact that $\left|z_n\right| = x_n$, it is possible to show that

$$\frac{\left|J_{m+1/2}\left(z_n\right)\right|^2}{x_n} = \frac{2}{\pi}\left|j_m\left(z_n\right)\right|^2 \tag{84}$$

where $\bar{z}_n$ is the complex conjugate of z_n. Then using the relationship linking j_m to its derivative (Eq. 10.1.21 of [23])

$$zj_m'\left(z\right) = -\left(m+1\right)j_m\left(z\right) + zj_{m-1}\left(z\right), \tag{85}$$

one can show that

$$\frac{\partial}{\partial x_n}\left[\frac{\left|J_{m+1/2}\left(z_n\right)\right|^2}{x_n}\right] = -\frac{4\left(m+1\right)}{\pi x_n}\left|j_m\left(z_n\right)\right|^2 + \frac{4x_n}{\pi\Re\left(z_n\right)}\Re\left[j_{m-1}\left(z_n\right)j_m\left(\bar{z}_n\right)\right] \tag{86}$$

$$\frac{\partial}{\partial y_n}\left[\frac{\left|J_{m+1/2}\left(z_n\right)\right|^2}{x_n}\right] = -\frac{2\Im\left[z_n j_{m-1}\left(z_n\right)j_m\left(\bar{z}_n\right)\right]}{\pi\Re\left(z_n\right)} \tag{87}$$

$$\frac{\partial^2}{\partial y_n^2}\left[\frac{\left|J_{m+1/2}\left(z_n\right)\right|^2}{x_n}\right] = -\frac{y_n \Im\left[z_n j_{m-1}\left(z_n\right) j_m\left(\bar{z}_n\right)\right]}{2\pi\Re\left(z_n\right)^3} + \frac{x_n^2\left|j_{m-1}\left(z_n\right)\right|^2}{\pi\Re\left(z_n\right)^2}$$

$$-\frac{\Re\left[2z_n j_{m-1}\left(z_n\right) j_m\left(\bar{z}_n\right) + z_n^2 j_{m-2}\left(z_n\right) j_m\left(\bar{z}_n\right)\right]}{\pi\Re\left(z_n\right)^2} \tag{88}$$

$$\frac{\partial^2}{\partial x_n \partial y_n}\left[\frac{\left|J_{m+1/2}\left(z_n\right)\right|^2}{x_n}\right] = -\frac{2x_n}{\pi\Re\left(z_n\right)^2}\left\{-\frac{\Im\left[z_n j_{m-1}\left(z_n\right) j_m\left(\bar{z}_n\right)\right]}{\Re\left(z_n\right)}\right.$$

$$+\Im\left[\left(1 - m - \frac{z_n^2}{x_n^2}\left(m+1\right)\right) j_{m-1}\left(z_n\right) j_m\left(\bar{z}_n\right)\right]$$

$$\left.+\Im\left[z_n j_{m-2}\left(z_n\right) j_m\left(\bar{z}_n\right)\right] + \Im\left(z_n\right)\left|j_{m-1}\left(z_n\right)\right|^2\right\} \tag{89}$$

Case $\Re\left(z_n\right) = 0$

When $\Re\left(z_n\right) = 0$, i.e. when $4x_n^2 < y_n^2$, it is convenient to replace the Bessel functions of first kind occurring in Eq.33 by modified Bessel functions of first kind of same order and real arguments by using the property

$$\left|J_{m+\frac{1}{2}}\left(z_n\right)\right|^2 = I_{m+\frac{1}{2}}\left(z_n^+\right) I_{m+\frac{1}{2}}\left(z_n^-\right) \tag{90}$$

where

$$z_n^{\pm} = \frac{1}{2}\left(y_n \pm \sqrt{y_n^2 - 4x_n^2}\right) \tag{91}$$

One can use the property (Eq.10.2.12. of [23])

$$I_{m+\frac{1}{2}}\left(x\right) = \sqrt{\frac{2x}{\pi}}\mathcal{G}_m\left(x\right) \tag{92}$$

with

$$\mathcal{G}_m\left(x\right) = g_m\left(x\right)\sinh\left(x\right) + g_{-m-1}\left(x\right)\cosh\left(x\right) \tag{93}$$

which is valid for any integer m and real argument x. The functions g_m are defined by recurrence as $g_0\left(x\right) = x^{-1}$, $g_1\left(x\right) = -x^{-2}$ and

$$g_{m-1}\left(x\right) - g_{m+1}\left(x\right) = \left(2m+1\right) g_m\left(z\right)/z. \tag{94}$$

The first values of $g_m\left(x\right)$ are given in Tab 2. Using the fact that $z_n^+ z_n^- = x_n^2$, one gets

$$\frac{\left|J_{m+\frac{1}{2}}\left(z_n\right)\right|^2}{x_n} = \frac{2}{\pi}\mathcal{G}_m\left(z_n^+\right)\mathcal{G}_m\left(z_n^-\right) \tag{95}$$

It is possible to show that

$$\frac{\partial}{\partial x_n}\left[\frac{\left|J_{m+\frac{1}{2}}\left(z_n\right)\right|^2}{x_n}\right] = \frac{4x_n\left[\mathcal{G}_m'\left(z_n^-\right)\mathcal{G}_m\left(z_n^+\right) - \mathcal{G}_m'\left(z_n^+\right)\mathcal{G}_m\left(z_n^-\right)\right]}{\pi\left(z_n^+ - z_n^-\right)} \tag{96}$$

$$\frac{\partial}{\partial y_n}\left[\frac{\left|J_{m+\frac{1}{2}}\left(z_n\right)\right|^2}{x_n}\right] = \frac{2\left[z_n^+\mathcal{G}_m'\left(z_n^+\right)\mathcal{G}_m\left(z_n^-\right) - z_n^-\mathcal{G}_m'\left(z_n^-\right)\mathcal{G}_m\left(z_n^+\right)\right]}{\pi\left(z_n^+ - z_n^-\right)} \tag{97}$$

$$\frac{\partial^2}{\partial y_n^2}\left[\frac{\left|J_{m+\frac{1}{2}}\left(z_n\right)\right|^2}{x_n}\right]=\frac{2}{\pi\left(z_n^+-z_n^-\right)^2}\left[\left(z_n^+\right)^2\mathcal{G}_m''\left(z_n^+\right)\mathcal{G}_m\left(z_n^-\right)\right.$$
$$\left.-\left(z_n^-\right)^2\mathcal{G}_m''\left(z_n^-\right)\mathcal{G}_m\left(z_n^+\right)-2x_n^2\mathcal{G}_m'\left(z_n^+\right)\mathcal{G}_m'\left(z_n^-\right)\right] \tag{98}$$

$$\frac{\partial^2}{\partial x_n\partial y_n}\left[\frac{\left|J_{m+\frac{1}{2}}\left(z_n\right)\right|^2}{x_n}\right]=\frac{4x_n}{\pi\left(z_n^+-z_n^-\right)^2}\left[\mathcal{G}_m'\left(z_n^+\right)\mathcal{G}_m\left(z_n^-\right)-\mathcal{G}_m'\left(z_n^-\right)\mathcal{G}_m\left(z_n^+\right)\right.$$
$$+y_n\mathcal{G}_m'\left(z_n^+\right)\mathcal{G}_m'\left(z_n^-\right)$$
$$\left.-z_n^+\mathcal{G}_m''\left(z_n^+\right)\mathcal{G}_m\left(z_n^-\right)-z_n^-\mathcal{G}_m''\left(z_n^-\right)\mathcal{G}_m\left(z_n^+\right)\right] \tag{99}$$

m	$g_m(x)$	m	$g_m(x)$
-5	$-105x^{-4}-10x^{-2}$	0	x^{-1}
-4	$15x^{-3}+x^{-1}$	1	$-x^{-2}$
-3	$-3x^{-2}$	2	$3x^{-3}+x^{-1}$
-2	x^{-1}	3	$-15x^{-4}-6x^{-2}$
-1	0	4	$105x^{-5}+45x^{-3}+x^{-1}$

Table 2. Values of $g_m(x)$ for low m integers

Appendix C: Velocity derivatives of $\tilde{\Theta}_{k,0}^n$

$$\frac{\partial\tilde{\Theta}_{k,0}^n}{\partial v_\parallel}=\frac{\left[\begin{array}{c}\left[1+\mathcal{C}_1\left(\theta_0\right)\right]J_{n+1}'\left(\tilde{\rho}_0\right)+\left[1-\mathcal{C}_1\left(\theta_0\right)\right]J_{n-1}'\left(\tilde{\rho}_0\right)\\-2\mathcal{C}_2\left(\theta_0\right)\frac{v_\parallel}{v_\perp}J_n'\left(\tilde{\rho}_0\right)\end{array}\right]}{2\sqrt{1+\mathcal{C}_1\left(\theta_0\right)^2+\mathcal{C}_2\left(\theta_0\right)^2}}\frac{\partial\tilde{\rho}_0}{\partial v_\parallel}$$
$$-\frac{\mathcal{C}_2\left(\theta_0\right)J_n\left(\tilde{\rho}_0\right)}{v_\perp\sqrt{1+\mathcal{C}_1\left(\theta_0\right)^2+\mathcal{C}_2\left(\theta_0\right)^2}} \tag{100}$$

$$\frac{\partial\tilde{\Theta}_{k,0}^n}{\partial v_\perp}=\frac{\left[\begin{array}{c}\left[1+\mathcal{C}_1\left(\theta_0\right)\right]J_{n+1}'\left(\tilde{\rho}_0\right)+\left[1-\mathcal{C}_1\left(\theta_0\right)\right]J_{n-1}'\left(\tilde{\rho}_0\right)\\-2\mathcal{C}_2\left(\theta_0\right)\frac{v_\parallel}{v_\perp}J_n'\left(\tilde{\rho}_0\right)\end{array}\right]}{2\sqrt{1+\mathcal{C}_1\left(\theta_0\right)^2+\mathcal{C}_2\left(\theta_0\right)^2}}\frac{\partial\tilde{\rho}_0}{\partial v_\perp}$$
$$+\frac{\mathcal{C}_2\left(\theta_0\right)v_\parallel J_n\left(\tilde{\rho}_0\right)}{v_\perp^2\sqrt{1+\mathcal{C}_1\left(\theta_0\right)^2+\mathcal{C}_2\left(\theta_0\right)^2}} \tag{101}$$

where

$$\frac{\partial\tilde{\rho}_0}{\partial v_\parallel}=\frac{\sin\left(\theta_0\right)\mathcal{N}\left(\theta_0\right)\omega_b}{\Omega_e c}\frac{v_\perp v_\parallel}{c^2}\gamma^3 \tag{102}$$

$$\frac{\partial\tilde{\rho}_0}{\partial v_\perp}=\frac{\sin\left(\theta_0\right)\mathcal{N}\left(\theta_0\right)\omega_b}{\Omega_e c}\gamma\left[1+\left(\frac{v_\perp\gamma}{c}\right)^2\right] \tag{103}$$

References

[1] S. Coda, S. Alberti, P. Blanchard, T. P. Goodman, M. A. Henderson, P. Nikkola, Y. Peysson, and O. Sauter. Electron cyclotron current drive and suprathermal electron dynamics in the TCV tokamak. *Nuclear Fusion*, 43(11):1361–1370, 2003.

[2] P. Nikkola, O. Sauter, R. Behn, S. Coda, I. Condrea, T. P. Goodman, M. A. Henderson, R. W. Harvey, and the TCV team. Modelling of the electron cyclotron current drive experiments in the TCV tokamak. *Nuclear Fusion*, 43(11):1343–1352, 2003.

[3] Y. Peysson, J. Decker, L. Morini, and S. Coda. RF current drive and plasma fluctuations. *Plasma Physics and Controlled Fusion*, 53(12):124028, 2011.

[4] J. Decker, Y. Peysson, and S. Coda. Effect of density fluctuations on eccd in iter and tcv. *EPJ Web of Conferences*, 32:01016, 2012.

[5] H. Weber, O. Maj, and E. Poli. Scattering of diffracting beams of electron cyclotron waves by random density fluctuations in inhomogeneous plasmas. *EPJ Web of Conferences*, 87:01002, 2015.

[6] A. Snicker, E. Poli, O. Maj, L. Guidi, A. Köhn, H. Weber, G. Conway, M. Henderson, and G. Saibene. The effect of density fluctuations on electron cyclotron beam broadening and implications for ITER. *Nuclear Fusion*, 58(1):016002, 2017.

[7] A. Köhn, L. Guidi, E. Holzhauer, O. Maj, E. Poli, A. Snicker, and H. Weber. Microwave beam broadening due to turbulent plasma density fluctuations within the limit of the born approximation and beyond. *Plasma Physics and Controlled Fusion*, 60(7):075006, may 2018.

[8] O. Chellaï, S. Alberti, M. Baquero-Ruiz, I. Furno, T. Goodman, B. Labit, O. Maj, P. Ricci, F. Riva, L. Guidi, E. Poli, and the TCV team. Millimeter-wave beam scattering by edge-plasma density fluctuations in TCV. *Plasma Physics and Controlled Fusion*, 61(1):014001, nov 2018.

[9] O. Chellaï, S. Alberti, I. Furno, T. Goodman, O. Maj, G. Merlo, E. Poli, P. Ricci, F. Riva, and H. Weber. Millimeter-wave beam scattering and induced broadening by plasma turbulence in the TCV tokamak. *Nuclear Fusion*, 61(6):066011, apr 2021.

[10] D. Choi, S. Coda, J. Decker, J. A. Cazabonne, and Y. Peysson. Study of suprathermal electron dynamics during electron cyclotron current drive using hard x-ray measurements in the TCV tokamak. *Plasma Physics and Controlled Fusion*, 62(11):115012, oct 2020.

[11] P. Donnel, J. Cazabonne, L. Villard, S. Brunner, S. Coda, J. Decker, M. Murugappan, and M. Sadr. Quasilinear treatment of wave–particle interactions in the electron cyclotron range and its implementation in a gyrokinetic code. *Plasma Physics and Controlled Fusion*, 63(6):064001, apr 2021.

[12] E. Lanti, N. Ohana, N. Tronko, T. Hayward-Schneider, A. Bottino, B.F. McMillan, A. Mishchenko, A. Scheinberg, A. Biancalani, P. Angelino, S. Brunner, J. Dominski, P. Donnel, C. Gheller, R. Hatzky, A. Jocksch, S. Jolliet, Z.X. Lu, J.P. [Martin Collar], I. Novikau, E. Sonnendrücker, T. Vernay, and L. Villard. Orb5: A global electromagnetic gyrokinetic code using the pic approach in toroidal geometry. *Computer Physics Communications*, 251:107072, 2020.

[13] F. Albajar, N. Bertelli, M. Bornatici, and F. Engelmann. Electron-cyclotron absorption in high-temperature plasmas: quasi-exact analytical evaluation and comparative numerical analysis. *Plasma Physics and Controlled Fusion*, 49(1):15–29, 2006.

[14] Y. Peysson, J. Decker, and L. Morini. A versatile ray-tracing code for studying rf wave propagation in toroidal magnetized plasmas. *Plasma Physics and Controlled Fusion*, 54(4):045003, mar 2012.

[15] D. Estève, X. Garbet, Y. Sarazin, V. Grandgirard, T. Cartier-Michaud, G. Dif-Pradalier, P. Ghendrih, G. Latu, and C. Norscini. A multi-species collisional operator for full-f gyrokinetics. *Physics of Plasmas*, 22(12):122506, 2015.

[16] Y. Peysson and J. Decker. Numerical simulations of the radio-frequency-driven toroidal current in tokamaks. *Fusion Science and Technology*, 65(1):22–42, 2014.

[17] P. Donnel, C. Gheller, S. Brunner, L. Villard, E. Lanti, N. Ohana, and M. Murugappan. Moment approach of the multi-species nonlinear coulomb collision operator adapted to particle-in-cell codes. *Plasma Physics and Controlled Fusion*, 2021.

[18] B. J. Braams and C. F. F. Karney. Conductivity of a relativistic plasma. *Physics of Fluids B: Plasma Physics*, 1(7):1355–1368, 1989.

[19] C. F. F. Karney. Fokker-planck and quasilinear codes. *Computer Physics Reports*, 4(3):183 – 244, 1986.

[20] T. Görler, N. Tronko, W. A. Hornsby, A. Bottino, R. Kleiber, C. Norscini, V. Grandgirard, F. Jenko, and E. Sonnendrücker. Intercode comparison of gyrokinetic global electromagnetic

modes. *Physics of Plasmas*, 23(7):072503, 2016.

[21] O. Sauter, S. Brunner, D. Kim, G. Merlo, R. Behn, Y. Camenen, S. Coda, B. P. Duval, L. Federspiel, T. P. Goodman, A. Karpushov, A. Merle, and TCV Team. On the non-stiffness of edge transport in l-mode tokamak plasmas. *Physics of Plasmas*, 21(5):055906, 2014.

[22] R. Prater. Heating and current drive by electron cyclotron waves. *Physics of Plasmas*, 11(5):2349–2376, 2004.

[23] M. Abramowitz and I. A. Stegun, editors. *Handbook of Mathematical Functions with Formulas, Graphs, and Mathematical Tables.* U.S. Government Printing Office, Washington, DC, USA, tenth printing edition, 1972.